

A Gaussian-process-model-based approach for robust, independent, and implementation-agnostic validation of complex multi-variable measurement systems: application to SAR measurement systems

Cédric Bujard, Esra Neufeld, Mark Douglas, Joe Wiart, Niels Kuster

Abstract

Resource-efficient and robust validation of complex measurement systems that would require millions of test permutations for comprehensive coverage is an unsolved problem. In the paper, a general, robust, trustworthy, efficient, and comprehensive validation approach based on a Gaussian Process model (GP) of the test system has been developed that can operate system-agnostically, prevents calibration to a fixed set of known validation benchmarks, and supports large configuration spaces. The approach includes three steps that can be performed independently by different parties: 1) GP model creation, 2) model confirmation, and 3) model-based critical search for failures. The new approach has been applied to two systems utilizing different measurement methods for compliance testing of radiofrequency-emitting devices according to two independent standards, i.e., IEC 62209-1528 for scanning systems and IEC 62209-3 for array systems. The results demonstrate that the proposed measurement system validation is practical and feasible. It reduces the effort to a minimum such that it can be routinely performed by any test lab or other user and constitutes a pragmatic approach for establishing validity and effective equivalence of the two measurement device classes.

1. Introduction

In the context of harmonizing and improving different standardized validation procedures for specific absorption rate (SAR) measurement systems – systems that are used for compliance testing of radiofrequency-emitting devices such as mobile phones – key requirements have been identified to ensure reliable, independently-verifiable, implementation-agnostic, and comprehensive validation in large parameter spaces. For that purpose, a general, Gaussian Process model (GP model)-based approach has been developed and is under discussion for adoption in upcoming standards revisions. This approach, which will be elaborated and demonstrated in this paper, is believed to be widely applicable, i.e., well beyond SAR system validation, in situations where similar validation requirements exist.

GP modeling has been used before in the context of SAR safety assessment, but for a very different purpose, namely to reduce the number of electromagnetic simulations required to study the relationship between wave incidence angle and exposure [20].

1.1. SAR Measurement Systems and Standards

SAR measurement systems measure the exposure of the user to electromagnetic fields transmitted by a wireless device. Due to the close proximity of the wireless device to the user, some of these fields are absorbed in the user's body. In a SAR measurement system, the user's body is represented by a dielectric, tissue-simulating-medium-filled, human-shaped phantom, and one or more probes measure the electric field (E-field) inside the phantom while the wireless device is positioned next to it. At any location in the phantom, the SAR is related to the root-mean-squared value of the induced E-field, \vec{E} , in the medium through the relation below, where σ is the frequency-dependent electrical conductivity and $\rho = 1000 \text{ kg/m}^3$ is the mass density of the medium.

$$SAR = \frac{\sigma |\vec{E}|^2}{\rho}$$

The induced E-field is temporally and spatially assessed in the phantom. Then, spatial and time averaging of the SAR is applied, followed by the identification of the peak spatial- and time-averaged SAR (psSAR). This value is compared against the psSAR limits set by safety standards such as the International Commission on Non-Ionizing Radiation (ICNIRP), which have been adopted by many regulators. ICNIRP limits are also endorsed by the European Council [12] and adopted in the harmonized standards of the European Committee for Electrotechnical Standardization (CENELEC) [7] [8]. Before a wireless device can be sold on the market, the manufacturer is required to demonstrate that the psSAR is below the limit in all tested conditions defined by the measurement standard. ICNIRP

has set a psSAR limit of 2 W/kg averaged over a 10 gram cubic mass, applicable to the general public for localized exposures of the head and torso at frequencies from 100 kHz to 6 GHz [14]. Some countries, such as Canada, India and USA, have adopted a more stringent SAR limit of 1.6 W/kg averaged over a 1-gram cubic mass in accordance with the IEEE Standard C95.1-1999 [18]. Other limits apply to the limbs, and there are different limits for occupational exposure and whole-body exposure.

Two independent SAR measurement standards have been developed by the International Electrotechnical Commission (IEC) that are each largely based around one of two different SAR measurement technologies: scanning systems and array systems (the Supporting Information provides background on these two systems). IEC/IEEE 62209-1528 [15] applies to scanning systems that use a robot to scan a probe and directly measure the field with high resolution, and it is based on a standard that was released in 2001 and has been updated several times to account for changes in wireless technology, measurement system technology, and regulatory requirements. It is broadly accepted by national regulatory agencies. IEC 62209-3 [16], in contrast, applies to fixed array systems that rely on field reconstruction from sparse measurement data (using typically on the order of thousand sensors). It was released in 2019, but regulators have faced difficulties adopting it. For instance, CENELEC pointed out the lack of and need for formal equivalence between IEC/IEEE 62209-1528 and IEC 62209-3.

1.2. Validation of SAR Measurement Systems

Both standards include validation requirements. IEC/IEEE 62209-1528 [15] requires validation of each system component separately and has proven to be very robust. However, such an approach was not applicable in IEC 62209-3 [16] as array systems are implemented as sealed boxes without access to the different components, necessitating a different approach. Furthermore, array systems inherently have a much larger number of degrees-of-freedom (and potential sources of failure), due to the large number of sensors that are independently calibrated for the large number of power levels, frequencies, and modulations needed to accurately measure any mobile wireless communication signal. The standards committee was faced with the issue that a comprehensive set of tests would include millions of configurations, which cannot be practically implemented. The reduced set of standardized exposure conditions required by IEC 62209-3 [16] needs to be improved, as comparison studies using different array systems show large deviations in the measured SAR (as much as 5 dB [17, 36]).

In IEC 62209-3 [16], a pass-fail test was introduced by defining the maximum permissible error (MPE):

$$MPE = 10 \cdot \log_{10}(1 + u_{system} + u_{source}) \quad (1)$$

whereby u_{system} is the expanded uncertainty (i.e., the uncertainty for two standard deviations, giving a 95 % confidence interval) of the measurement system that shall be smaller than 30% and u_{source} is the expanded uncertainty of the target SAR value of the source and set to 15%. The 15% value was generously set and was added as a correlated uncertainty contribution in order to lower the burden of meeting the validation. To pass the validation, each validation configuration j must satisfy the following:

$$\left| 10 \cdot \log_{10} \left(\frac{SAR_{measured,j}}{SAR_{target,j}} \right) \right| \leq MPE,$$

where $SAR_{measured,j}$ is the measured SAR value and $SAR_{target,j}$ is the verified numerical target SAR value for the specific configuration.

1.3. Requirements for Validation of SAR Measurement Systems

A validation method is needed that satisfies the following requirements, in order to establish equivalence of the standards and drive universal acceptance of SAR measurement systems, whatever the method they apply:

- it is universally applicable to any SAR measurement system (device agnostic),
- it can make use of knowledge of the measurement system to reduce validation effort,
- it ensures that any successfully validated system performs within the acceptable measurement accuracy (as prescribed by corresponding standards) for any wireless device,
- it empowers the test lab to confirm the validation independently of the system manufacturer,

- it identifies critical test conditions that maximize the likelihood of identifying inadequate measurement device performance,
- it can be performed with a reasonable effort, to permit re-validation on a periodic basis (or whenever hardware or software components of the system change, or the system is relocated),
- it comprehensively covers the space of all relevant exposure conditions and configurations,
- it is readily extendable as wireless technologies evolve.

To simultaneously satisfy the requirements of comprehensive coverage and reasonable effort, it is necessary to introduce a stochastic component to the approach. Using a subset of all validation conditions selected by a procedure involving stochastic elements each time the validation is performed avoids bias and ensures increasingly comprehensive coverage over time. It also has the added benefit of preventing system manufacturers from primarily calibrating the system in view of a priori known validation configurations such that it would pass the validation but exceed the system uncertainty.

Two commercially available SAR measurement systems are studied in this paper: the scanning system DASY8 that complies with IEC/IEEE 62209-1528 and the array system cSAR3D that complies with IEC 62209-3. Both systems are manufactured by Schmid & Partner Engineering AG (Zurich, Switzerland).

DASY8 uses a six-axis robot to mechanically scan a single electric field probe inside a standardized liquid-filled phantom [28]. The probe contains three orthogonal dipole sensors to measure the full field polarization at every measurement location [29]. The probe is calibrated using a novel sensor model calibration technique to ensure accuracy for different modulated signals [34]. Two scans are performed: a coarse planar scan to find the SAR peak, followed by a high resolution volumetric scan to determine the psSAR. The scanning parameters, phantom shape, liquid dielectric parameters, and other requirements are defined in IEC/IEEE 62209-1528 [15].

cSAR3D has a two-dimensional array of sensors inside a gel-filled phantom [10]. The dielectric parameters of the gel adhere to the same requirements as for the DASY8, but the absence of moving parts permits the use of a gel instead of a liquid, to prevent ingredient separation over time in the sealed cSAR3D. Three cSAR3D phantoms are combined to represent the torso (flat phantom), and the left and right sides of the head. The flat phantom that is studied in this paper uses a total of 1024 sensors covering a measurement area of 120 mm x 240 mm. The sensors directly measure three orthogonal electric field components. The sensor model calibration technique employed for DASY8 [34] is again used to accurately handle signal modulation. Sensors are calibrated *in situ* in the final assembly, to compensate for uncertainties related to manufacturing tolerances.

1.4. A Three-Step Validation Approach

This paper presents a three step approach that satisfies all the above requirements and demonstrates its successful application to both scanning systems and array systems. At its center is the elaboration of a computational model that estimates the expected measurement error (and the confidence interval associated with that estimate) of the investigated system for a given exposure configuration. As this model is typically generated over an underlying GP, it will henceforth be referred to as the ‘GP model’. Note that the GP model is a model of the measurement system error and not of the measurement output itself.

The method consists of three independent steps, which are each described in detail in corresponding *Method* sections:

- 1) GP model creation: elaboration of the GP model using a comprehensive set of measurements,
- 2) GP model confirmation: independent confirmation that the GP model established in Step 1 is valid. Otherwise, the GP model must be revised,
- 3) Critical search for failures: search of the configuration space for critical regions (configurations with non-negligible likelihood of failing to meet the MPE), using the confirmed GP model to maximize detection probability, and testing the identified configurations to ensure that the measurement system performs with the required accuracy.

In the context of SAR measurement system validation, model creation would typically be performed by the system manufacturer, independent model confirmation by a test lab or the system user, and

the critical search for failures by an accredited test lab (at least once per year; the acceptable effort is believed to be in the order of 1 day).

The application of the developed approach to a scanning system and an array system demonstrates the feasibility (with acceptable effort), sensitivity, and generality of the proposed approach. Indeed, the method is sufficiently general to be of value in a wide variety of applications beyond SAR systems that require critical, independent, and efficient validation of system performance.

This method has been proposed for adoption in the next revision of IEC 62209-3 and for a future unified standard that incorporates both IEC 62209-3 and current IEC/IEEE 62209-1528.

1.5. Study Goals

The principal goal of this study is to identify and demonstrate a practical, robust, trustworthy, efficient, and comprehensive solution 1) to the specific problem of SAR system validation and 2) to the more general one of efficiently and reliably validating systems with a large configuration space in an unbiased, implementation-agnostic, and independently verifiable manner that maximizes the likelihood of detecting failure to ensure performance within the accepted error margin. It is *not* the goal to develop novel GP modeling theory (other than the extensions needed for the search algorithms, such as the $\delta_p(l)$ function derived in the Supporting Information), nor to identify the best possible approach to GP model construction, validation, and exploitation – this is an advanced field and the here applied methods were selected purely based on accessibility and effectiveness for the task at hand. At the same time, the employed approach has the important quality of only requiring a very small number of measurements for a high dimensional parameter space while respecting the practical constraints of being non-iterative (i.e., all measurements are performed in a single session).

2. Methods

This section presents the background of the proposed approach, before introducing the investigated generic and real world applications. It builds upon the test configuration space of IEC 62209-3 and IEC/IEEE 62209-1528.

2.1. GP Model

The Supporting Information provides background on GP modeling theory and also detailed introduction of the employed formalism and notations. Key notations include the Gaussian process $Y = \{Y(x) : x \in X\}$ of random variables $Y(x) = Y_x : X \rightarrow \mathbb{R}$ over a closed connected index set $X \subset \mathbb{R}^n$, a *semivariogram* $\gamma(h)$ with a finite and well defined *sill* $s_\gamma = \lim_{|h| \rightarrow \infty} \gamma(h)$ with the corresponding *range* r_γ at which $s_\gamma - \gamma(h)$ becomes negligible (typically below 5 % of s_γ), and a potentially non-zero nugget n_γ (see Fig 1).

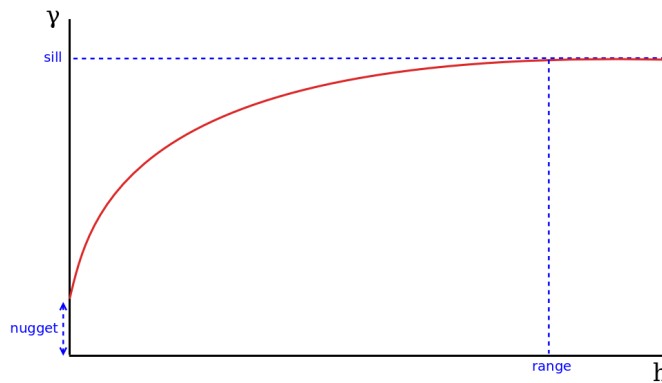


Figure 1: **Schematic illustration of a semivariogram.** The nugget, sill, and range are indicated.

Many GP construction approaches exist and can be employed, as long as they are capable of conservatively estimating variances and the model validation is successful. For this study, the matheron estimator for the semi-variance is used, with a gaussian model for the theoretical variogram, and the default fitting algorithm with the default class binning method from the SciKit-GStat package [22] are

employed, but alternative choices, e.g., of the semi-variogram curve model or the fitting algorithm, could have been equally suitable.

2.2. Model Creation using Latin Hypercube Sampling

In order for the initial sample S to efficiently generate a GP model, in the sense that a minimal number of points is used to build a satisfactory model, sample S needs to be well spread over domain X . The choice made was to use *Latin Hypercube Sampling (LHS)* [24, 27]. Background and implementation information can be found in the Supporting Information.

2.3. Model Confirmation

Given a GP model, the goal of this step is to establish a statistical validation procedure after which the model is to be either rejected or considered trustworthy. This procedure shall be referred to as the *model confirmation* procedure; it can be performed as a series of successive tests, with each success leading to the next test, where the model is considered valid if and only if the procedure reaches its end. The procedure can be divided into two main phases: *goodness of fit* and *residuals validation*. Statistical model validation is well studied field and valuable information can be found, e.g., in [30]. The metrics and tests chosen for this study are commonly employed in statistics.

2.3.1. Goodness of Fit

This section deals with assessing how well the theoretical semivariogram γ fits an empirical semivariogram $\hat{\gamma}$ built from the sample set \bar{S} of known values. The goal here is to check the coherence, i.e., the goodness of fit, of the variance model with respect to empirical knowledge. Here a measure of how well γ fits the empirical semivariogram $\hat{\gamma} = \{\hat{\gamma}_i\}_{i=1}^k$ computed from \bar{S} is needed. For each $i = 1, \dots, k$ one defines γ_i to be the value returned by γ at the lag corresponding to $\hat{\gamma}_i$. The *mean absolute error* (MAE) and the *root mean square error* (RMSE) are most often used in regression analysis to evaluate model accuracy:

$$\text{MAE} = \frac{1}{k} \sum_i |\hat{\gamma}_i - \gamma_i|, \quad \text{RMSE} = \sqrt{\frac{1}{k} \sum_i (\hat{\gamma}_i - \gamma_i)^2}.$$

These however depend on the scale of the variogram sill. The RMSE has the advantage of putting more emphasis on the tails of the residuals distribution. As a measure of goodness of fit, the *normalized root mean square error* (NRMSE) is used

$$\text{NRMSE} = \frac{\text{RMSE}}{\text{mean}(\hat{\gamma})} = \frac{\sqrt{k \sum_i (\gamma_i - \hat{\gamma}_i)^2}}{\sum_i \hat{\gamma}_i}, \quad (2)$$

whose magnitude does not depend on the sill. The GP model passes the goodness of fit test when $\text{NRMSE} \leq \alpha$ for a given acceptance value α (typically in the interval $[0.1, 0.3]$, see *Parameter Choices*).

2.3.2. Residuals Validation

This section evaluates how a well fitted model generalizes to other samples $\bar{T} \subset X \times \mathbb{R}$. In practice, such a test sample is obtained either as the test subset of a train-test cross validation partition of a larger known sample, or as a set of measurements acquired independently from the initial sample that was used to build the model. The residuals of T against a model are the differences between the measured values $y(x)$ and the corresponding predictions $\hat{y}(x)$. If the model matches the data correctly, the residuals $e(x)$ approximate those random errors that make the relationship between x and y a statistical relationship. Therefore if the residuals appear to behave randomly and follow the expected distribution, it suggests that reality is successfully modeled. On the other hand, if non-random structure is evident in the residuals, or if their distribution is inadequate, it is a sign that the model poorly fits reality.

The validity of the model is evaluated based on a well distributed test sample \bar{T} such that $T \cap S = \emptyset$. For every $x \in X$, the kriging function returns a pair $(\hat{y}(x), \hat{e}(x))$, where $Y(x)$ knowing $Y(S)$ follows a

normal distribution of mean $\hat{y}(x)$ and variance $\hat{e}(x)^2$. Because $\hat{y}(x)$ is an unbiased linear combination of the elements of $y(S)$ with $\hat{e}(x)^2$ the variance $\text{Var}(\bar{Y}(x) - Y(x))$, the random variable

$$\bar{Y}(x) = \frac{Y(x) - \hat{y}(x)}{\hat{e}(x)} \sim \mathcal{N}(0, 1). \quad (3)$$

follows the standard normal distribution. Consequently, many well known statistical tests are applicable. The suggested procedure is as follows:

- 1) Set T so that $T \cap S = \emptyset$ and T contains 50 elements that are evenly distributed across X with a local identically independently distributed (*iid*) component,
- 2) Use the Shapiro-Wilk (SW) test (see [32]) to determine the normality of $\bar{Y}(T)$ with acceptance $\alpha = 0.05$,
- 3) Make a QQ-plot of $\bar{Y}(T)$ versus $\mathcal{N}(0, 1)$ on the $[0.025, 0.975]$ inter-quantile range,
- 4) As the plot is expected to be linear based on the above step, use the QQ-location μ (the QQ value at zero) and the QQ-scale (the QQ values slope) σ to determine standard normality with acceptance $|\mu| \leq 1$ and $0.5 \leq \sigma \leq 1.5$.

See *Parameter Choices* regarding the choice of an appropriate T , as well as the acceptance thresholds. A bad QQ-location indicates a bad T or a poorly calibrated model. The QQ-scale is the standard deviation of the residuals relative to the ideally expected standard deviation of $\mathcal{N}(0, 1)$. Slope values below the ideal 1.0 are an indication of model conservativeness (overestimation) and thus are more acceptable than values above 1.

2.4. Critical Search for Failures

Given a fully confirmed GP model, the goal becomes to search the entire domain X for regions containing points x that have non-negligible probabilities for $Y(x)$ to cross a given threshold; these are referred to as *critical regions* that contain *critical data points*. As X might have a relatively high dimension n (higher than the $n = 2$ or 3 typically encountered in geostatistics), a good GP model might require a relatively large initial sample S , which can lead to substantially slower kriging interpolation computations. It is therefore essential to establish an algorithm that identifies the critical regions of X efficiently. This requires an algorithm that exploits the available information – as contained in the GP model – to perform its task. The proposed algorithm relies on the *delta measure*, which is introduced next.

2.4.1. The Delta Measure

The Supporting Information includes a derivation of a novel function $\delta_p(l)$ that permits to estimate for a given point x_0 in X , how far away the next candidate point x must be to have a reasonably likelihood of $Y(x)$ crossing the threshold T . It is found that being $l > 0$ away from T , this distance is

$$\delta_p(l) = \begin{cases} 0 & \text{if } l \leq g_p(n_\gamma), \\ \gamma^{-1} \left(\frac{1}{2} \left(\frac{l}{\Phi^{-1}(p)} \right)^2 \right) & \text{if } g_p(n_\gamma) < l < g_p(s_\gamma), \\ r_\gamma & \text{if } l \geq g_p(s_\gamma), \end{cases} \quad (4)$$

where Φ is the normal cumulative density function, and $g_p(d) = \sqrt{2d}|\Phi^{-1}(p)|$ for a parameter $0 < p < \frac{1}{2}$.

Knowing the values T and $y_0 = Y(x_0)$ at x_0 , one can choose a parameter p and use $\delta_p(T - y_0)$ to find the closest points to x_0 with a probability $\geq p$ to cross the threshold T . The function δ_p , as illustrated in Fig 2, encodes all the covariance characteristics carried by the variogram. p expresses the sensitivity of the model in the assessment of whether or not the true value $y(x)$ is considered to have crossed T . The smaller p (i.e., faster fluctuations are handled), the shorter the distance $h = |x - x_0|$ at which the system suspects T to potentially have been crossed, and hence the smaller $\delta_p(l)$ become.. On the other hand, when p tends towards $\frac{1}{2}$, its most extreme value, the function δ_p reacts increasingly slowly to changes of h , up to the point where it no longer makes use of the information content of γ . As y_0 approaches T , $\delta_p(l)$ approaches zero in accordance with γ . When $|T - y_0|$ is larger than $g_p(s_\gamma)$, x is too far away from x_0 for the condition $Y(x_0) = y_0$ to have an influence on the outcome of $Y(x)$.

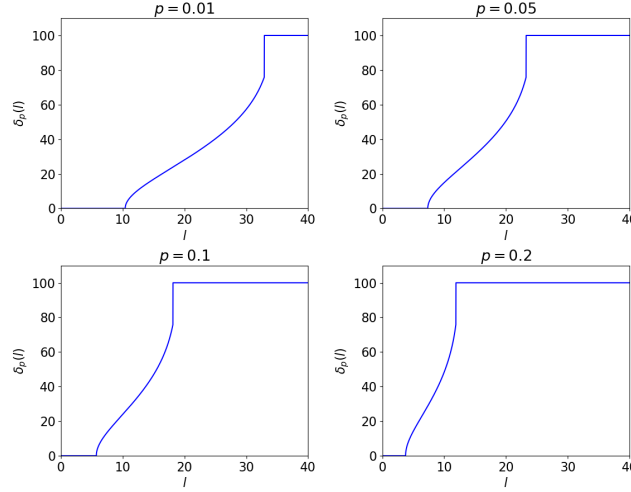


Figure 2: **The delta function $\delta_p(l)$.** It permits to estimate for a given point x_0 in X , how far away the next candidate point x must be to have a reasonable likelihood of $Y(x)$ crossing the threshold T . $\delta_p(l)$ is shown here for different values of the sensitivity p , where the range and sill of the semivariogram are fixed to 100 and the nugget to 10 ($r_\gamma = s_\gamma = 100$ and $n_\gamma = 10$). With decreasing p the expected fluctuation rate increases, resulting in increased interpolation uncertainty and a need to remeasure at smaller distances.

δ_p can only be effectively incorporated into an algorithm, if it can be efficiently evaluated at any x . This only depends on the ability to efficiently evaluate the inverse function γ^{-1} on the interval (n_γ, r_γ) . Even though computing the inverse of a function is in general computationally intensive (provided it even exists), the most commonly used variogram models, including the one used here, happen to be analytically invertible (see Eq 8, 9 and 10).

2.4.2. Search Algorithm

The proposed search algorithm is motivated by heuristic optimization methods, with an added uncertainty component. Its goal is to identify critical configurations to be remeasured (search for global extrema), rather than estimating the probability of failure or improving the surrogate model. The considerations that went into designing the search algorithm were that it must: 1) maximize the chance of detecting configurations with a high likelihood of exceeding the MPE, while minimising the number of required measurements; 2) balance the need to spread coverage of the search space, against the need to increase the sampling density if either the response surface fluctuates strongly, or if the predicted measurement error is close to the MPE such that even small fluctuations could result in a violation of the MPE; 3) adhere to the general philosophy of established validation procedures from the currently binding standard (point-by-point evaluation according to a pass-fail criterion, with a single fail invalidating the system); and 4) converge rapidly and be amenable to efficient implementation.

The function δ_p can be used to build an efficient search algorithm for identifying critical regions in which Y is likely to cross given threshold(s). Let $S_0 \subset X$ be a finite, evenly distributed sample over X – such an S_0 can for example be a well designed random latin hypercube. Let f be a realization of Y over its domain $X = \mathcal{D}(f)$; it can for example be a kriging function built from the elements of S_0 . Let $T_-, T_+ \in \mathbb{R}$ denote two thresholds such that $T_- < T_+$. At the i th iteration, the search algorithm produces a new sample $S_i \subset X$ in such a way that the series (S_i) converges towards a sample that is evenly distributed over (non connected) critical regions. An element of $\{S_i\}$ is denoted S_* , and T_* denotes an element of $\{T_-, T_+\}$, where $*$ acts as a general placeholder. Using δ_p , setting the algorithm parameter q to p , and for a small number of iterations $m \geq 1$, algorithm 1 returns a new sample S_m in which points of S_* have been moved towards local extrema of f in such a way that they are evenly spread throughout the regions that are likely to be close to or beyond the upper and lower thresholds T_\pm .

Algorithm 1 is a search trajectory method that modifies the elements of population S_* according to two kinds of forces:

- A force that pulls x such that $y(x)$ is pulled towards the nearest T_\pm . Once $Y(x)$ crosses that

Algorithm 1 Search algorithm

```
1: procedure SEARCH( $S_* \in X, f : X \rightarrow \mathbb{R}, T_-, T_+, \delta_p : \mathbb{R}_+ \rightarrow \mathbb{R}_+, q \in [0, 1], m \in \mathbb{N}^*$ )
2:    $Y_* = f(S_*)$ 
3:    $T_0 = (T_- + T_+)/2$ 
4:    $d = -1, s = 0$ 
5:   for  $k = [1, m]$  do
6:      $\alpha = \frac{1}{2k}$ 
7:     for  $j = [0, |S_*|)$  do
8:        $x_j = S_*[j], y_j = Y_*[j]$ 
9:       if  $y_j > T_0$  then
10:         $d = (y_j > T_+) ? \alpha\delta_p(y_j - T_+) : 2\alpha\delta_p(T_+ - y_j)$ 
11:         $s = 1$ 
12:       else
13:         $d = (y_j < T_-) ? \alpha\delta_p(T_- - y_j) : 2\alpha\delta_p(y_j - T_-)$ 
14:         $s = -1$ 
15:        $S'_* = \{x_j\} \cup \{x_j \pm d\vec{e}_i \in X : i = [1, \dim(x)]\}$ 
16:        $Y'_* = f(S'_*)$ 
17:        $D'_* = (\min_{x \in S_* \setminus \{x_j\}} \{|x - x'|\} : x' \in S'_*)$ 
18:        $h = \operatorname{argmax}_i \{s(Y'_*[i] - T_0) \cdot D'_*[i]^{\frac{q}{2}}\}$ 
19:        $S_*[j] = S'_*[h], Y_*[j] = Y'_*[h]$ 
20:   return  $S_*, Y_*$ 
```

threshold, x 's velocity decreases and starts converging towards a nearby extrema of Y . The force is a function of $\delta_p(|y(x) - T|)$ for T the closest threshold,

- A mutually repulsive force that serves to spread the elements of S_* and quickly decreases with distance. The force on any x_0 is a function of its distance to the set $S_* \setminus \{x_0\}$. This prevents points from converging towards the same configuration: they should cover regions of interest in a way that maximizes their minimal separation.

Assuming that f also returns its estimation uncertainty for $y(x)$, that is $f(x) = (\mu_x, \sigma_x)$ where $\sigma_x = 0$ if $f = y$, one can use algorithm 2 to return the two subsets $L_*, U_* \subset S_*$ of points that have a probability of at least p to cross the corresponding thresholds.

Algorithm 2 filters out the elements of S_* whose probability of crossing the nearest threshold is lower than p . The kriging error is used as the volatility of Y at x . Points are grouped into those that are below T_- with a probability of at least p , those that are above T_+ with a probability of at least p , and the remaining points, which are returned together with their probability of exceeding either threshold.

Algorithm 2 Filter algorithm

```
1: procedure FILTER( $S_* \in X, f : X \rightarrow \mathbb{R} \times \mathbb{R}_+, T_-, T_+, p \in [0, 1]$ )
2:    $L_* = \emptyset, U_* = \emptyset, M_* = \emptyset, P_* = \emptyset$ 
3:    $a = \Phi^{-1}(p)$ 
4:   for  $x \in S_*$  do
5:      $\mu_x, \sigma_x = f(x)$ 
6:     if  $\mu_x < T_-$  and  $a \leq (T_- - \mu_x)/\sigma_x$  then
7:        $L_* = L_* \cup \{x\}$ 
8:     else if  $\mu_x > T_+$  and  $a \leq (\mu_x - T_+)/\sigma_x$  then
9:        $U_* = U_* \cup \{x\}$ 
10:    else
11:       $M_* = M_* \cup \{x\}, P_* = P_* \cup \min \left\{ \Phi \left( \frac{T_- - \mu_x}{\sigma_x} \right) + \Phi \left( \frac{\mu_x - T_+}{\sigma_x} \right), 1 \right\}$ 
12:   return  $L_*, U_*, M_*, P_*$ 
```

2.4.3. Initial Population

The initial population is again selected using LHS, which is computationally efficient, well suited in combination with the search algorithm, and was found to be effective. The Supporting Information provides a criterion for selecting the S_0 sample size required for the search algorithm to either locate out of bound elements, or – if none are found – to establish confidence that there are none:

$$\nu_p = \prod_{i=1}^n \left\lceil \frac{\sup(X_i) - \inf(X_i)}{\delta_p(\bar{l})} \right\rceil, \quad (5)$$

where X_i is the projection of X on its i th dimension ($1 \leq i \leq n = \dim(X)$). It is evident that the choice of p affects ν_p . It reflects effort-reliability-balance considerations and ensures that the algorithm detects threshold violations with a user-defined sensitivity level.

2.5. Applications

The developed validation methodology has been applied to (1) an analytic example where the underlying model is known, such that the successful ability of the proposed method to identify critical configurations can be assessed, (2) a subspace of the system validation of cSAR3D to gain an understanding of the performance of the proposed approach, and full system validation of (3) cSAR3D and (4) DASY8. In applications (3) and (4), care was taken to ensure that GP model creation was performed independently of the model confirmation and the critical search for failures by involving two different measurement laboratories, LAB1 (IT'IS Foundation, Switzerland) and LAB2 (BNN, India), with different operators and different sets of equipment (sources and measurement systems). GP model creation was performed by LAB2, and GP model confirmation and critical search for failures were performed by LAB1.

Note that for application (1), an analytical function is used with the goal of identifying regions where the function exceeds given thresholds. Application (2)–(4) deal with measurement reliability, and hence the GP model is constructed and tested against deviations between measured values and target values. It is important to emphasize that the goal is *not* to predict SAR, but to predict the SAR measurement error and to identify configurations where that error is likely to exceed the MPE tolerance.

The four applications of the validation methodology, along with the elaboration of the exposure configuration space, are now described.

2.5.1. Analytic Benchmark Example

This section illustrates how the search algorithm works on a simple example for which the underlying realization is fully known. Let $S \subset X = [0, 1]^2$ be the 2-dimensional LHS sample shown in Fig 3, and let $Y : X \rightarrow \mathbb{R}$ be such that

$$Y(x) = f(x) + e, \quad \text{where} \quad f(x) = y \sin(2\pi y), \quad y = \frac{1}{\sqrt{2}}|x|, \quad e \sim \mathcal{N}(0, 0.001^2).$$

This process is isotropic and the semivariogram model γ is Gaussian with parameters $r_\gamma = 0.97$, $s_\gamma = 0.22$, $n_\gamma = 0$ (obtained numerically; see Fig 4).

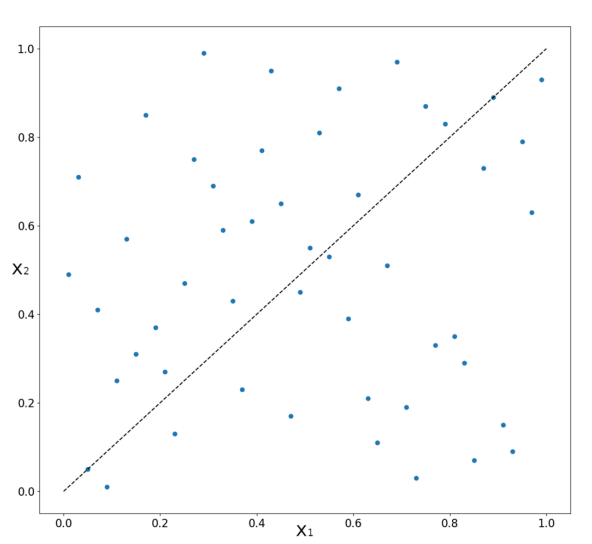


Figure 3: **Latin square sample $S \in [0, 1]^2$ of size 50.** The diagonal line is illustrated in the function reconstruction in Fig 5.

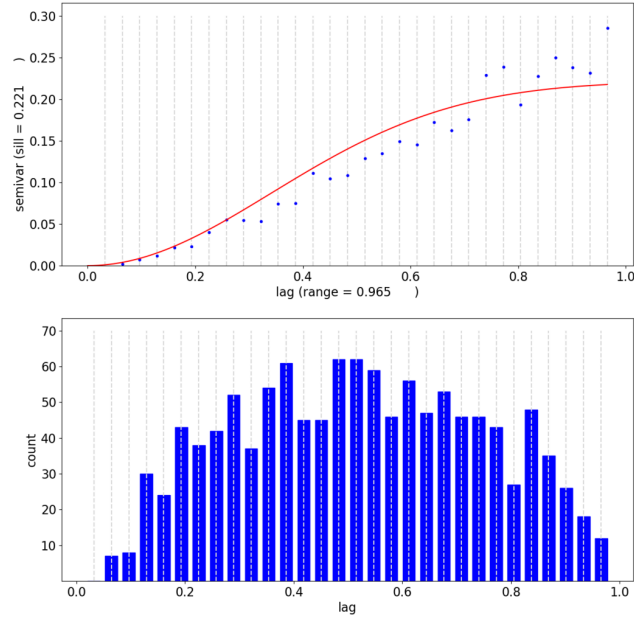


Figure 4: **Isotropic semivariogram for the sine wave analytical benchmark.** It is shown along with the binning histogram used in its construction. Importantly, the number of samples in the transition region of the semivariogram is sufficient to capture its shape.

Kriging was applied to this model on the segment line $\{\lambda(1,1) : \lambda \in [0, 1]\}$ depicted in black in Fig 3. The search algorithm was applied with varying sensitivities p and iterations m , while fixing the threshold $T_{\pm} = \pm 0.75$ and reusing S as initial sample set, even though a new (and frequently larger) sample set would typically be used.

2.5.2. Dimensions and Range of Parameter Space for cSAR3D and DASY8 Validation

For SAR measurement system validation, the dimensions of the sampling space must cover all relevant variables for system validation, and each dimension must cover a range sufficient to validate the system for foreseeable exposure conditions. This section describes the relevant variables that parameterize the configuration space for SAR measurement system validation. The Supporting Information describes

their ranges and the practical realization of the configuration set for which the relevant standards [15, 16] provide reference values.

The measurement accuracy of a SAR measurement system depends on the following SAR parameters:

Frequency: The calibration of the SAR measurement system is frequency-dependent, due to the dispersion of the tissue-simulating medium dielectric parameters and the frequency response of the system components (e.g., amplifiers, filters). Typically, the sensors are calibrated at discrete frequencies and the calibration is interpolated to cover entire bands.

SAR level: The accuracy of the measured SAR is dependent on the SAR level, due to non-linearities of the SAR measurement system that are compensated through calibration. Therefore, the system needs to be validated across the system's dynamic range.

Polarization: The system must measure the induced E-field for any polarization. A measurement system might do this using multiple, e.g., orthogonally-oriented, sensors inside the probe that can be combined to isotropically sense arbitrary field orientations. Imperfect isotropy, i.e., angle-of-incidence-dependence, affects the measurement uncertainty and needs to be considered in the validation. To address all combinations, different sources and varying orientations are defined:

- 1) sources with a dominant polarization parallel to the phantom surface (e.g., dipole antenna) which are rotated at different angles with respect to the the phantom surface normal. This tests the accuracy of the x - and y -component measurements.
- 2) sources with a dominant polarization normal to the phantom surface (e.g., Vertically-Polarized Planar Inverted F Antenna, VPIFA [16]) to test the accuracy for the z -component.

SAR pattern: The measurement accuracy can depend strongly on the spatial distribution of the SAR, e.g., due to sensor design, spatial resolution, sensor distance to the phantom surface – which affects the capability to reliably measure rapidly decaying fields – and the use of reconstruction algorithms. The measurement system must be validated with sources that cover the range of potential SAR distributions from wireless devices.

Modulation: Probes are calibrated using different modulated signals commonly employed in wireless devices (e.g., 3G, 4G, 5G, and WLAN signals). The signal bandwidth, BW (in MHz) is an important signal parameter in the frequency domain, while the peak-to-average ratio (PAR , in dB) and the duty cycle (in %) describe signal aspects in the time domain.

Location: Array systems must be validated at any x and y locations within the measurement boundaries, because the measured SAR varies due to a) mechanical tolerances and calibration errors of the different probes in the array, b) measurement variations related to the discrete field sampling by the probes, and c) the influence of field scattering across the probe array that may be different in the center of the array compared to the array boundaries.

To validate a SAR measurement system while accounting for the above aspects requires testing of the system using validation field sources placed in close proximity to the phantom surface. A set of standardized validation sources is available to the test lab or system manufacturer lab. These sources operate at different frequencies f and have different SAR patterns. The operator can also create different SAR patterns by adjusting the distance s of the source to the phantom, and the rotational angle θ with respect to the phantom normal. The signal is fed to the source at different input power levels, P_{in} , using modulations with different peak-to-average ratios (PAR) and bandwidths (BW). For array systems, the location (x, y) on the phantom can be changed to test all of the probes in the array, while scanning system use a single measurement probe (potentially with multiple sensors). These are the eight dimensions of the validation space (six for scanning systems) that the operator can select from. The relationships between these variables and the validation parameters described above are shown in Table 1 and further explained in the Supporting Information.

These eight dimensions are believed to be a sufficient set for the system validation of general SAR measurement systems, while six dimensions are sufficient for scanning systems due to their independence on the device location (x, y) , as explained before. Knowledge about the SAR measurement system implementation could be used to further reduce the number of dimensions and of required validation measurements. For example if the scanning system implementation is independent of the rotation of the SAR pattern, the sampling of the rotation angle θ could be reduced or removed. Or, the dimensions

Variable	Validation parameter	Variable range
Frequency, f (with antenna type)	SAR pattern polarization (normal) frequency	15 dipoles 300 – 5800 MHz, 4 VPI-FAs at 750, 835, 1950, 3700 MHz, 1 dual-peak CPIFA at 2450 MHz
Distance, s	SAR pattern	dipoles at 5, 10, 15, 25 mm, VPI-FAs at 2 mm, CPIFA at 7 mm
Rotation angle, θ	SAR pattern polarization (tangential)	$0^\circ - 360^\circ$, in 15° steps
Location, x	location (array systems)	any point along width in 1 mm steps
Location, y	location (array systems)	any point along length in 1 mm steps
Input power, P_{in}	SAR level	CW: $SAR_{1g} = 1 - 100$ W/kg in 1 dB steps, modulated: $SAR_{1g} = 0.1 - 10$ W/kg in 1 dB steps
PAR	modulation	0 – 12 dB
BW	modulation	0 – 100 MHz

Table 1: **Configuration space used for SAR measurement system validation.** There are eight dimensions for array systems and six for scanning systems due to the independence of scanning systems on location (x and y). See Table 3 regarding the signals used to sample the modulation, PAR, and BW dimensions

of frequency f and distance s could be reduced and/or combined for a high-resolution scanning system that is less sensitive to the SAR pattern. Still it must be kept in mind that both characteristics of the measurement system as well as of its reconstruction algorithms must be considered. For this study, the authors chose to maintain the full dimension space to demonstrate device dependence on all parameters.

Note that each of these dimensions is continuous by nature. Reduction to a finite number of measurable configurations is only the result of practical limitations in validation hardware (primarily the number of exposure dipole sources).

2.5.3. cSAR3D (x, y, θ) -subcube

We first examine the case of SAR deviations measurements on the (x, y, θ) -subdomain of a cSAR3D device (fixing the other parameters). The initial set is composed of 25 locations $L = \{(x_i, y_i)\}_{i \in [1, 25]}$ randomly selected among the vertices of the canonical 3 mm lattice of the measurable surface. For each location (x_i, y_i) , the set of 12 angles $A = \{15j \bmod 180 : j \in [0, 11]\}$ in degree is considered, and the initial sample set is set to be

$$S = L \times A = \{(x_i, y_i, 15j)\} \subset X \subset \mathbb{R}^3,$$

under the constraints that a single dipole antenna is used at an operating frequency of 2450 MHz that is fed with a continuous-wave signal with zero PAR and zero BW, at powers in the range of 25 – 36 dBm, and with the source placed at a fixed distance of $s = 10$ mm to the phantom.

2.5.4. cSAR3D Validation

For the full cSAR3D system validation, the entire validation procedure was performed, this time covering the complete configuration space described above.

Model Creation:. A GP model for the full configuration space was constructed from a set measurements on a cSAR3D flat phantom measured at LAB2.

Initial sample generation: An initial sample S of 400 data points (see *Parameter Choices*) was LHS-generated with a maximization of the minimal distance between any two points, so as to ensure that S was well spread within X . For the chosen configurations the 1g-averaged SAR (SAR_{1g} [16, 15]) was measured using a cSAR3D device (flat phantom), and the corresponding deviations ΔSAR_{1g} from the target values were computed, resulting in the valued sample \bar{S} .

Outlier detection: Potential outliers were detected and their measurement values double checked. An *outlier* is defined to be any value not in the set

$$\{ x \in S : y(x) \in [q_1 - r(q_3 - q_1), q_3 + r(q_3 - q_1)] \},$$

where q_1, q_3 are the first and third quartiles of $y(S)$, and where r is a positive predetermined interquartile range multiplier chosen equal to 2 in this case. With $r = 2$, few valid values might still be outliers. Outliers are not to be ignored from the linear system of equations used for interpolation, but they are to be ignored during the construction of the final isotropic variogram.

Model creation: The data space was prescaled based on the standard deviations of the known values $y(S) = Y(S)$ along each dimension; i.e., for $Y(S)_i$ the projection of $Y(S)$ on the 1-dimensional \mathbb{R} -subvector space generated by the i -th variable unit, and for s_i the standard deviation of $Y(S)_i$, the invertible linear map ι_0 is pre-constructed as the diagonal matrix

$$\Sigma_0 = \begin{pmatrix} s_1 & & 0 \\ & \ddots & \\ 0 & & s_n \end{pmatrix}.$$

Working from $\iota_0(X)$ not only normalizes the arbitrary choice of units, but also reduces the conical uncertainties in the construction of the 1-dimensional directional variograms along each dimension (lag pairs are chosen with a certain angular tolerance around the direction-of-interest to improve the statistics). In the present case, the Gaussian shape from Fig 1 is used for the variogram fitting and, due to the very different characteristic length of each variable's variation, only the range, sill and nugget need to be determined along the eight directions of the canonical base vectors of the surrounding space \mathbb{R}^n . Importantly, the sill has to be similar along all directions and the nugget has to be close to zero. As this was the case for the cSAR3D measurements, ι is defined as the composition

$$\Sigma = \begin{pmatrix} r_1 & & 0 \\ & \ddots & \\ 0 & & r_n \end{pmatrix} \cdot \Sigma_0,$$

where r_i is the range of the directional variogram along dimension i . Now that $\iota(X)$ is isotropic, an 8-dimensional semivariogram γ on $\iota(X)$ can be estimated.

Model Confirmation: The GP model was confirmed by 50 independent measurements taken at LAB1 with different equipment and operator than those involved in the model creation performed at LAB2.

Good fit validation: It is asserted that the isotropic semivariogram γ fits the empirical semivariogram $\hat{\gamma}$ sufficiently well by quantifying its NRMSE value (an acceptance threshold of 25% was chosen, see *Parameter Choices*). Similarly to the generation of \bar{S} , a random test sample $\bar{T} = \{(x, Y(x)) : x \in T\} \subset \mathbb{R}^n \times \mathbb{R}$ of 50 points was generated, such that:

- T was independent from S with $S \cap T = \emptyset$,
- T was locally randomly uniformly distributed, in the sense that an element of T must be randomly picked within a predefined neighborhood (for example within its square in the case of an LHS-generated T).

This last point differs from S where global evenness (as opposed to local randomness) is a necessity. The evenness of T is less important, while its randomness is crucial. The independence between T and S is equally crucial. In the extremely unlikely case where some configurations x belongs to $S \cap T$ after generating T , they should not be used, or T should be resampled, as zero residuals are not allowed in the next phase. In this example, the same LHS generation algorithm was used as it satisfies the criteria for both S and T sampling. A test sample is recommended to contain at least 50 elements. If multiple GP models are to be compared the same test sample (or at least the same test sample size) should be used.

Residuals validation: The residuals are obtained from the values in \bar{T} using Eq 3. Provided T has good randomness, the residuals are to be standard normal distributed. The Shapiro-Wilk test with a p -value well above 0.05 did assert normality, and the QQ-plot of the order statistics of the residuals versus the theoretical standard normal distribution were assessed.

Critical Search for Failures:. The confirmed GP model was used to search the data space for critical regions where SAR deviations to the target values are likely to exceed the MPE. These critical cases were then measured to check whether or not the values exceed the MPE.

Search for critical sample: A sample of appropriate size and distribution was generated. Eq 5 was used to select the sample size, with minimum and maximum hard caps set at 10 and 1000, respectively. The sample used to initiate the search algorithm 1 was LHS-generated using the GP model. Eight iterations were performed and the configurations that have a probability of at least 5% to exceed the MPE thresholds were returned. After the last iteration, snapping to the closest meaningful neighbour is performed (see *Methodology and Implementation*).

Measurement of critical cases: The identified critical sample was measured on a cSAR3D flat phantom to determine whether the deviations in SAR_{1g} exceed the MPE. This was performed by LAB1 with different equipment and operator than those used by LAB2 for the model creation measurements.

2.5.5. DASY8 Validation

For the full DASY8 system validation, as in the case of cSAR3D, a GP model is constructed based on a LHS-generated initial set S augmented by system knowledge from the manufacturer. The opportunity to incorporate such knowledge without compromising the validation trustworthiness – thanks to the model confirmation step, which involves a physically measured test set T of 50 samples – is another important advantage of the proposed approach. The procedure for creating the GP model was identical to that of the cSAR3D case, except that a non-zero nugget was included as a model parameter since the nugget was found to be non-negligible compared to the sill.

Confirmation of the GP model and critical search for failures were conducted for DASY8 in the same way as for cSAR3D.

2.6. Methodology and Implementation

Selected implementation-specific aspects, such as parameter choices, are discussed here.

2.6.1. Parameter Choices

The proposed procedure involves a number of tuneable parameters:

- To establish the GP model based on a LHS-distributed initial sample, a size of 400 is usually needed to ensure that 75% of all bins used in the construction of the empirical semivariogram contain at least 40 lag values.
- The Gaussian semivariogram model was chosen from the smoothness of the underlying process (a result of the smooth dependence of the measurement physics on variations of the underlying parameters). It also has the advantage of being less sensitive to variance changes at the smallest lags where the LHS generated initial sample provides few to no values.
- A value in the range 10–30% is typically chosen for the NRMSE tolerance α in the fit validation of the model confirmation step. Data analysis has shown that an α below that range is too severe, while special care must be taken if values above that range are to be tolerated.
- As explained in [32], the SW test is best applied to samples that have 20-50 elements, while at least 50 points are recommended for the QQ-plot to be meaningful. The usual tolerance of 5% is applied; this could easily be increased for more severity, however, normality itself is less important than the scale and location factors of the QQ-test.
- The QQ-test location and scale tolerance are set at $|\mu| < 1$ and $0.5 \leq \sigma \leq 1.5$. In order to accept more conservative models, the tolerance for σ is much more permissive below than above the ideal 1.
- The constant of repulsion q in the search algorithm should typically be chosen in the range of 0.05–0.2, depending on the expected global smoothness of the SAR deviation behavior over the configuration space. A default value of 0.1 has been shown to work for both cSAR3D and DASY8,
- The number of iterations m in the search algorithm is set to 8 at which the produced sample stabilizes over the critical regions,

- The value of ν_p is in the range 50–10'000: The search algorithm can efficiently handle such a potentially large number of trajectories.

2.6.2. LHS Implementation

A custom LHS generation implementation inspired by that of pyDOE [2] was used: this variant provides control over the RNG seed. See the Supporting Information for more information on the LHS implementation.

2.6.3. Data Snapping

The search algorithm works within a continuous connected domains X . It generates an initial sample and moves all elements along their own trajectory. At every iteration, a sample in X is obtained. After the last iteration, all values are snapped to their euclidean closest meaningful value. A final kriging round is performed to estimate the likelihood of exceeding the threshold for the obtained configurations. In rare instances, if the resulting element x was too far from practically meaningful location, it is removed from the resulting critical set.

The general approach is to treat domain X as a continuous connected subset of \mathbb{R}^n , and to derive meaningful (i.e., on the raster from Table 1) values *a posteriori* (after the last iteration) through snapping to their closest meaningful neighbour. The source selection is based on the (frequency, distance)-pair. If a frequency is valid for different source types, distance is used as a secondary criterion. When no meaningful source exists, the sample point is ignored. This approach avoids having to treat categorical variables, discrete variables and continuous variables differently in the validation procedure, and therefore greatly simplifies all statistical operations without significantly affecting the results.

2.6.4. Variogram Modeling

All semivariograms shown here are generated using the scikit-gstat package from the pypi repository; all details on the methods used are provided in [22]. The Matheron semivariance estimator given in Eq 7 is used as empirical variogram. The Gaussian semivariogram model defined in Eq 9 was found to be the most effective model, especially when the nugget is small. The convex nature of the model at short ranges reduces the fitting uncertainty associated with the typically sparse sampling data at the shortest lags. The domain is binned such that 75% of its diameter is partitioned into 25 equally-sized bins for the 1-dimensional directional variograms and into 50 bins for the final isotropic variogram. An initial sample size of 400 is usually recommended (see *Parameter Choices*). While zero nugget models work for cSAR3D, it becomes obvious that nuggets are necessary in the DASY8 case. In fact, it is even possible to successfully model DASY8 systems with a flat variogram representing pure noise.

3. Results

3.1. Analytic Sine Wave Example

The fitted isotropic semivariogram of the GP model can be seen in Fig 4. Applying kriging using this model on the segment line $\{\lambda(1, 1) : \lambda \in [0, 1]\}$ depicted in black in Fig 3, Fig 5 is obtained, where the red curve is the exact noiseless function f , the blue curve is the estimated interpolation \hat{f} along with its 99 % confidence interval. The confidence interval decreases the closer one gets to a known value, and it increases where the sampling is sparser and towards the domain's border, where less data is available.

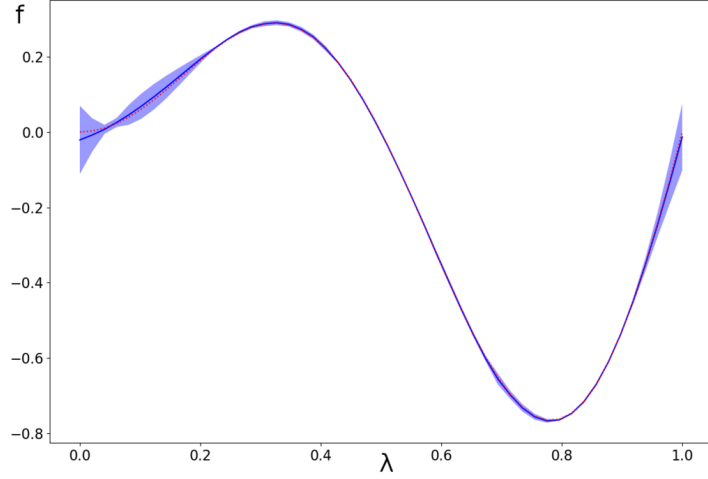


Figure 5: **Illustration of GP interpolation of noisy samples from an analytical benchmark (incl. confidence interval).** The estimated interpolation $\hat{Y}(x)$ along the diagonal from Fig 3 is shown. The red curve is the exact noiseless function f , the blue curve is the estimated interpolation \hat{f} along with the associated 99 % confidence interval.

The application of the search algorithms for various sensitivities p , and iterations m , moves the elements of S as illustrated in Fig 6 and Fig 7 respectively.

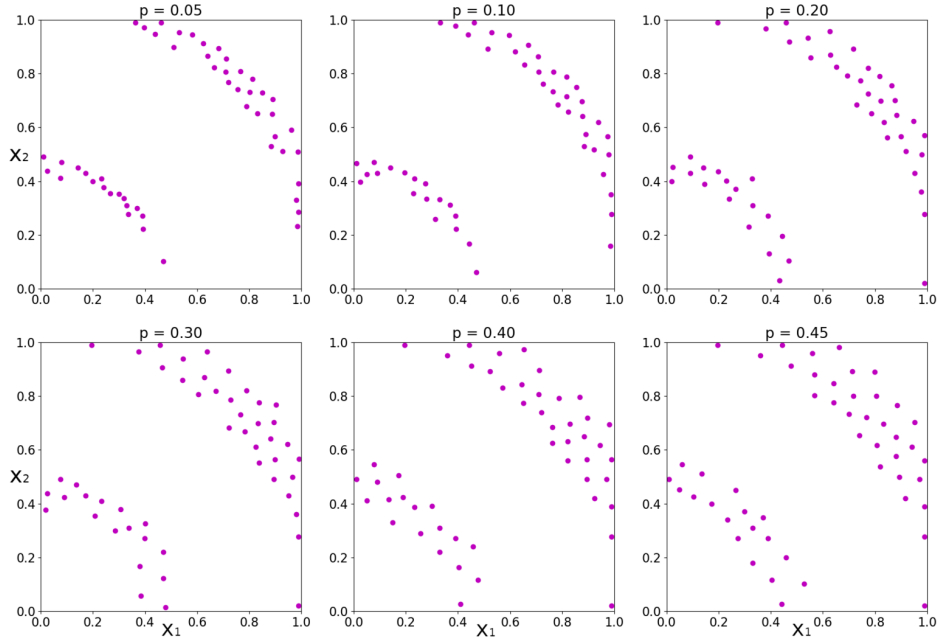


Figure 6: **Results obtained using algorithm 1 for the search for configurations at risk of exceeding the threshold.** The identified set of configurations are shown for various values of the sensitivity p (always with 8 iterations). A higher p reflects the expectation of a smoother response surface, which permits to increase the spacing between sampling points and to search the configuration space more coarsely.

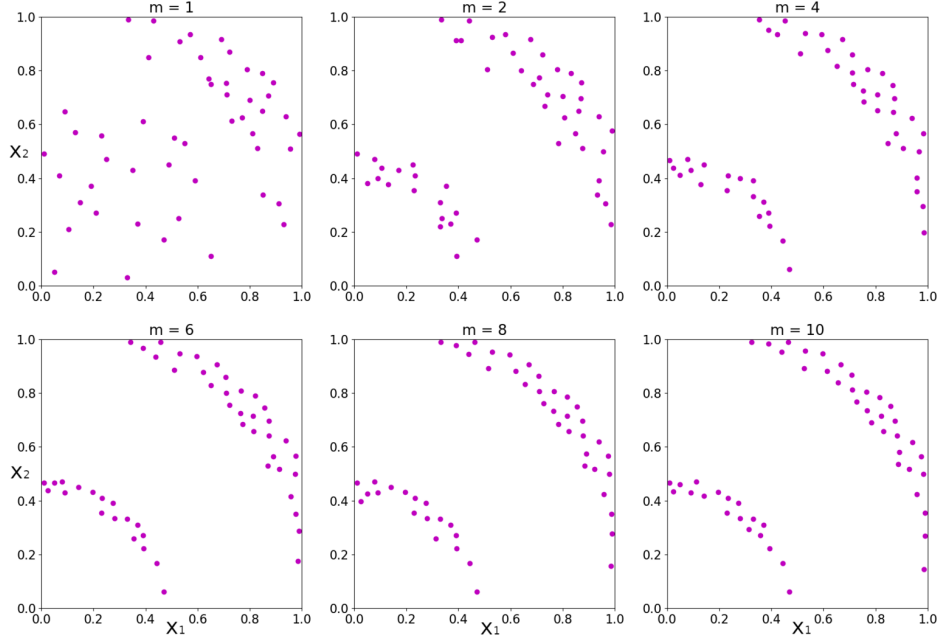


Figure 7: **Impact of the iteration number m on the results returned by algorithm 1.** The sensitivity parameter is set to $p = 0.1$ throughout with an increasing number of iterations m . Quick convergence up to $m = 8$, then stabilization beyond $m = 8$ of the resulting design is observed.

Each of these points come with their own probability to cross the thresholds. Fig 8 shows the result for $T_{\pm} = \pm 0.75$, T_- , which is identical to the infimum of f on X .

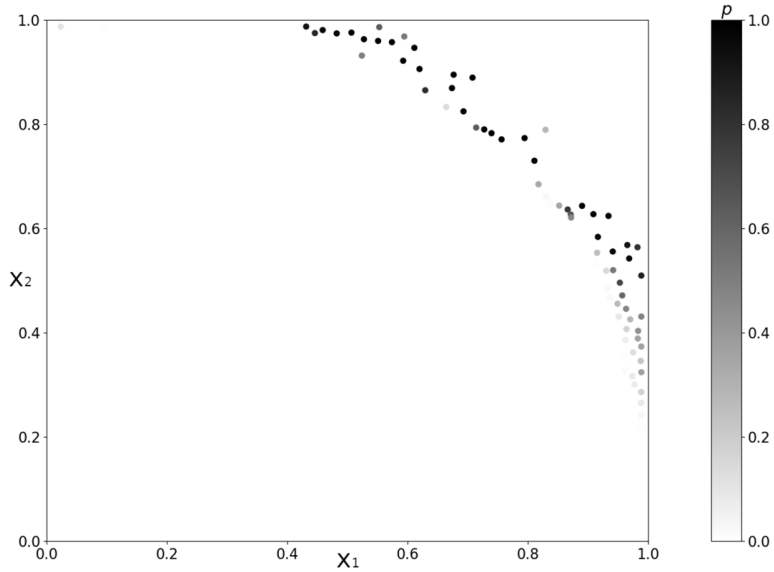


Figure 8: **Configurations for ‘remeasurement’ identified by the complete search procedure (algorithms 1 and 2).** The probability of the samples to fall below the lower threshold of $T_- = -0.75$ is indicated.

Note that:

1) The sensitivity p must be set according to the degree of smoothness and the rate of variation of f over its domain X : if p is chosen too small, points are overly likely to be classified as potentially crossing the thresholds T_{\pm} , potentially resulting in a too large number of requested measurements during the critical search for failures. On the other hand, if p is overly large, the crossing condition might not trigger rapidly enough to detect sharp peaks in f , potentially leading to undetected regions. The impact of the p value is illustrated in Fig 6.

- 2) The fact that δ_p incorporates the relevant semivariogram characteristics allows the algorithm to remain efficient with a minimal number of iterations (provided the semivariogram model is of high quality). Fig 7 illustrates how after only two iterations the points are already surrounding the searched regions.
- 3) In Fig 6 and Fig 7, the remarkable regularity in how points are set apart from each other is apparent. This is controlled by the parameter q , the constant of repulsion. In the analytic example, q is set to p which is often a good idea: with a lower p a finer search is performed and thus a repulsive force that decreases rapidly with distance is needed. For coarser searches over wider regions, points should not be too close to each other, and a higher q ensures that the repulsion acts on longer ranges. Setting $q = 0$ will remove any repulsion between points.
- 4) The search algorithm can be adapted in various ways. In the present example, knowing that S starts as a latin hypercube, the choice was made to search along each dimension of X , reducing the likelihood of multiple points colliding too quickly. If S was chosen to be a lattice with high regularity, one would rather use search trajectories that incorporate random element.

3.2. cSAR3D (x, y, θ) -subcube

The results from applying the developed procedure to the (x, y, θ) -subdomain of a cSAR3D device provide valuable insights into how regions can be identified that – as a result of the measurement system design (in this case, the arrangement of sensors in the probe array) – have an increased likelihood of exceeding the accuracy limits.

The set of measured configurations $\bar{S} = \{(x_k, y_k, \theta_k, y_k)\}$ can be represented by projecting all measurement deviations y_k onto each dimension: their mean and standard deviation are shown in Fig 9.

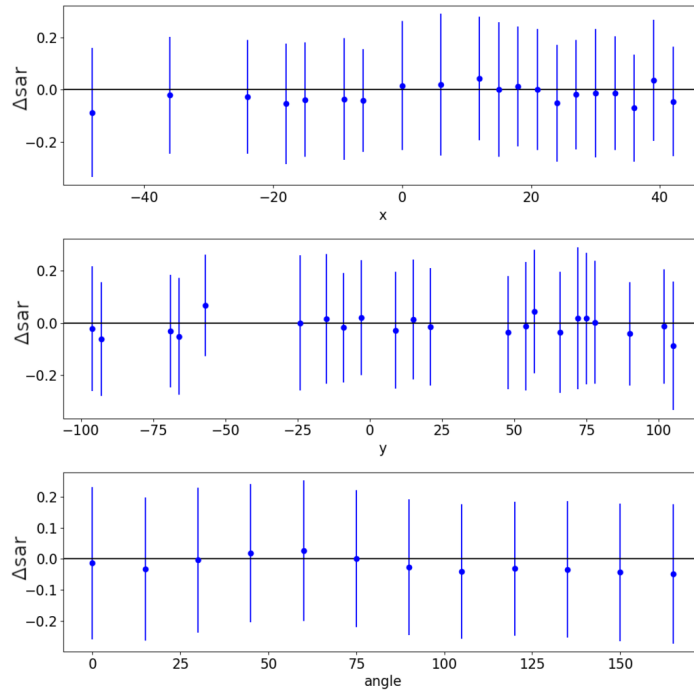


Figure 9: **The set \bar{S} of the measured cSAR3D deviations from the target values, projected along the different dimensions of the (x, y, θ) -subcube configuration space.** The bars denote the standard deviations of all elements of \bar{S} with the same projected parameter value.

Note that the locations are not as optimally distributed (i.e., locally random, but globally homogeneous) as if they would have been LHS-generated. This is compensated by the high number of elements in S and the high regularity of all standard deviations across the board. The data shows a smooth geometric anisotropy with low noise. The underlying data space X can easily be rescaled into an isotropic space $\iota(X)$ on which the obtained isotropic semivariogram γ shown in Fig 10.

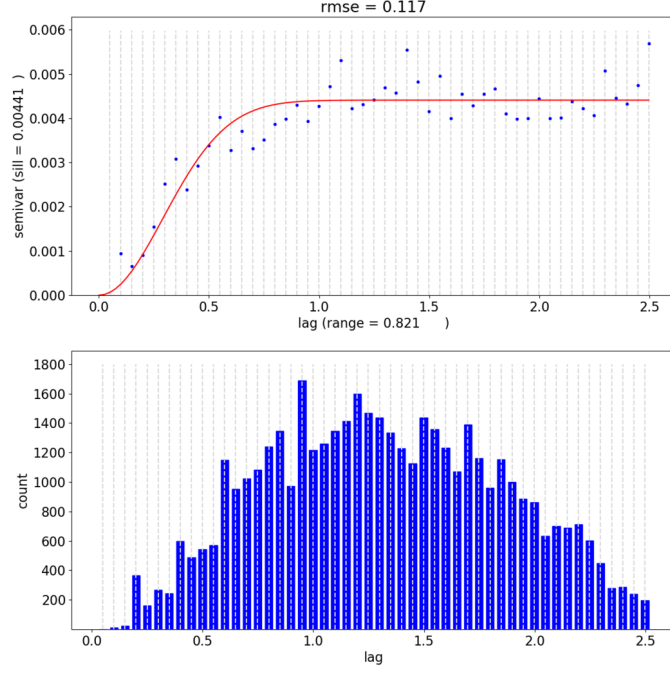


Figure 10: **Empirical (blue) and fitted (red) isotropic semivariogram for the cSAR3D system in the (x, y, θ) -subcube of the configuration space.** It is shown along with the histogram of the sample lags in the underlying bins. There are enough lags per bin (heuristic findings indicate that at least 30-50 are desirable) to perform a reliable parameters estimation of the semivariogram.

The NRMSE of less than 12% indicates that the semivariogram is well suited for probing X . Applying the search algorithm with a very low MPE threshold of 0.3 dB (well below that allowed by the standards; see Eq 1). using different sensitivity values p results (after only 8 iterations) in the critical samples shown in Fig 11. Color clustering is apparent in Fig 11, which corresponds to the local extrema along the θ dimension from Fig 9, namely 15, 65, 105, 120, 165 degrees. Fig 12 then applies algorithm 2 and returns the probability of exceeding the MPE value. Clear clustering around the global maximum at 65 degrees and the global minimum at 165 degrees is evident.

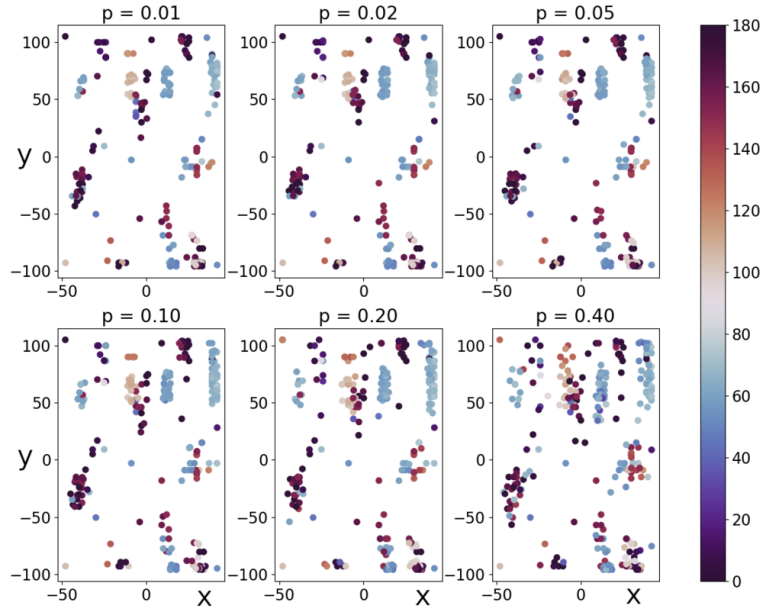


Figure 11: **Results obtained for the reduced cSAR3D dataset when applying the first step (algorithm 1) in the search for critical configurations.** The outcomes for various values of the sensitivity parameter p are shown on the (x, y) -surface, while encoding θ in color.

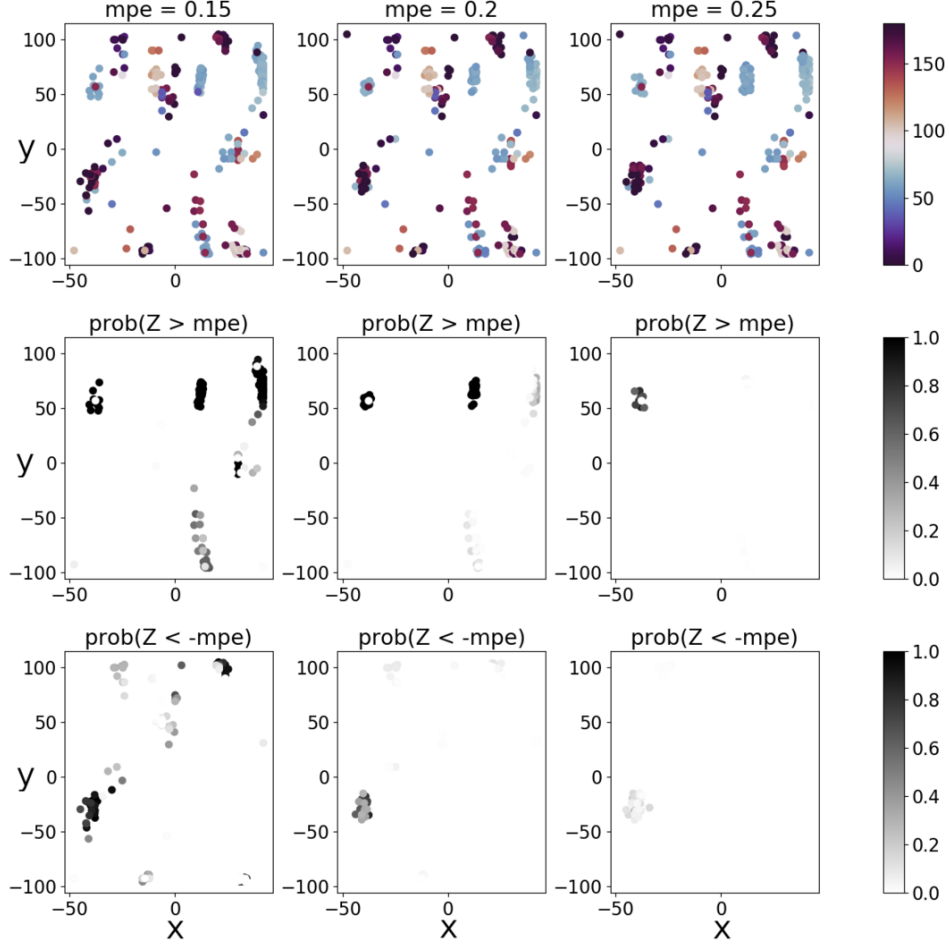


Figure 12: **Results obtained for the reduced cSAR3D dataset when applying the full search procedure to identify critical configurations.** Shown are the outcomes of algorithm 1 (top; see as well Fig 11), and of algorithm 2. The probabilities of exceeding a given error threshold (0.15, 0.2, or 0.25 dB, which is well below the MPE allowed by the standards; see Eq 1) from above (middle) and below (bottom) are also illustrated.

3.3. cSAR3D Validation

3.3.1. Model Confirmation

Good fit validation:. The isotropic semivariogram γ fits the empirical semivariogram $\hat{\gamma}$ with an NRMSE value below the acceptance threshold of 25%. Typically, a good model has an NRMSE in the range of 8% to 15%, which is the case here as shown in Fig 13. A higher NRMSE might still be acceptable in more extreme cases, provided the error resulting from the interpolation process takes this uncertainty into consideration: the following heuristic formula for the interpolation error has been found to be suitable

$$e(x) = e_k(x) \cdot (1 + \text{NRMSE}),$$

where $e_k(x)$ is the kriging error at x .

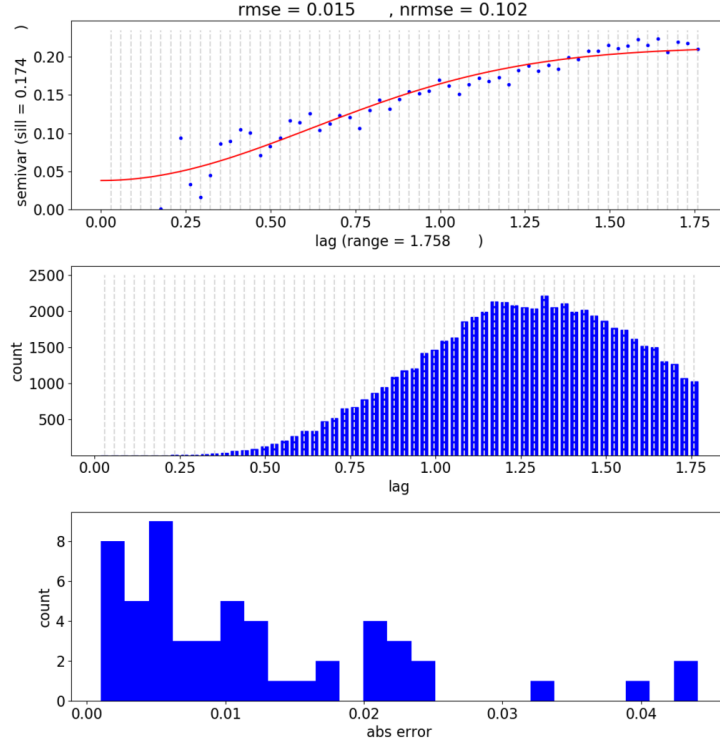


Figure 13: **Construction of the semivariogram of the cSAR3D GP model.** The semivariogram is shown along with the histogram of the binned sample lags used for its construction and the histogram of the absolute errors between the empirical variogram and the fitted theoretical one. The validation of the fit quality returned an NRMSE of about 10 %.

Residuals validation: The Shapiro-Wilk test confirms that the residuals are indeed normally distributed, with a p -value well above 0.05. As shown in Fig 14, the linear regression of the QQ-plot of the residuals order statistics versus the theoretical standard normal distribution has its location and scale well within $[-1, 1]$ and $[0.5, 1.5]$, respectively.

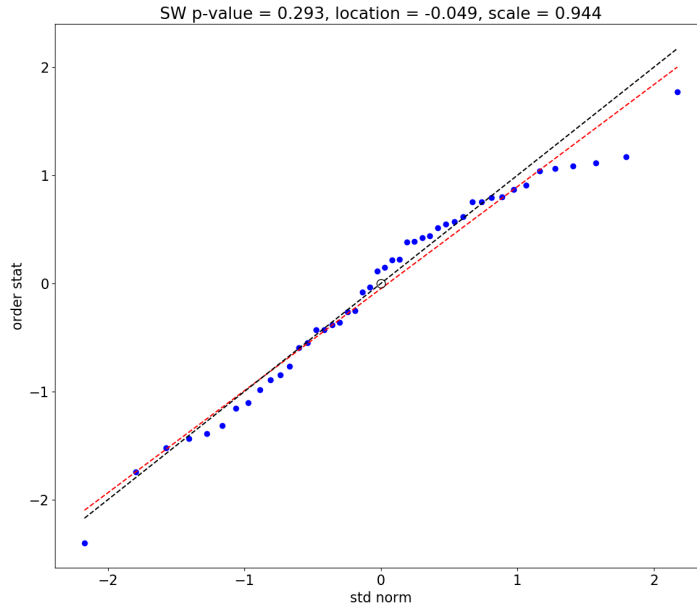


Figure 14: **Residuals QQ-plot of the cSAR3D model confirmation step.** The Shapiro-Wilk test p -value, as well as the location and scale of the linear regression are within their acceptance ranges, confirming the GP model.

3.3.2. Critical Search for Failures

The confirmed GP model was used to search the data space for critical regions. This is typically performed by an independent test lab to validate the device.

Search for Critical Configurations:. The critical configurations returned after 8 iterations of the search algorithm with an attributed probability of at least 5% to exceed the MPE value can be seen in Table 2. These configurations are sorted by decreasing probability of exceeding the MPE (from 18.8 % to 5.1 %). A cluster of cases using the D5000 dipole at a distance $s = 25$ mm with input power levels around $P_{in} = 10$ dBm is evident, as well as two cases using the V750 antenna. This is unsurprising, as the D5000 and V750 antennas have the sharpest SAR distributions among the sets of dipole antenna and VPIFA, respectively. A sharper SAR distribution results in a larger measurement variability for an array system with a fixed sensor resolution.

Ant. name	f (MHz)	P_{in} (dBm)	PAR (dB)	BW (MHz)	s (mm)	θ ($^\circ$)	x (mm)	y (mm)	ΔSAR_{1g} (dB)	Model error (dBm)	Failure prob. (%)
V750	750	9.0	3.98	5.0	2	90	-33.0	32.0	-1.249	0.282	18.8 %
D5000	5600	11.0	8.91	40.0	25	0	-46.0	-60.0	1.102	0.362	13.6 %
V750	750	9.0	5.67	20.0	2	75	-19.0	22.0	-1.161	0.284	11.6 %
D5000	5500	10.0	8.91	40.0	25	15	-46.0	-38.0	1.076	0.352	11.4 %
D5000	5500	13.0	8.91	40.0	25	15	-36.0	-68.0	1.102	0.329	11.3 %
D5000	5200	10.0	8.91	40.0	25	0	-26.0	-18.0	1.104	0.318	10.6 %
D5000	5500	10.0	8.43	25.0	25	15	-30.0	-19.0	1.108	0.313	10.5 %
D5000	5500	10.0	8.91	40.0	25	30	-35.0	-5.0	1.092	0.326	10.5 %
D5000	5500	18.0	7.93	0.4	25	15	-43.0	59.0	1.056	0.352	10.4 %
D5000	5600	13.0	8.43	25.0	25	15	-22.0	-53.0	1.106	0.300	9.4 %
D5000	5800	16.0	9.38	20.0	25	45	-14.0	-85.0	1.084	0.313	9.2 %
D5000	5500	11.0	8.91	40.0	25	15	-12.0	-80.0	1.077	0.316	9.0 %
D5000	5800	15.0	8.43	25.0	25	30	-6.0	-89.0	1.093	0.302	8.9 %
D5000	5500	11.0	9.38	20.0	25	15	-31.0	53.0	1.063	0.323	8.8 %
D5000	5600	15.0	6.59	10.0	25	0	-34.0	-44.0	1.094	0.299	8.7 %
D5000	5800	8.0	10.28	100.0	25	15	-7.0	-28.0	0.969	0.388	8.6 %
D5000	5800	8.0	8.90	80.0	25	45	-15.0	-40.0	1.022	0.335	7.7 %
D5000	5500	10.0	10.28	100.0	25	30	-13.0	3.0	0.954	0.379	7.5 %
D5000	5600	10.0	10.28	100.0	25	60	-1.0	14.0	0.950	0.380	7.4 %
D5000	5800	23.0	8.43	25.0	25	15	-48.0	-32.0	0.994	0.345	7.1 %
D5000	5800	8.0	8.90	80.0	25	30	-26.0	72.0	0.904	0.406	7.1 %
D5000	5500	10.0	8.91	40.0	25	15	-43.0	68.0	0.973	0.357	7.0 %
D5000	5800	11.0	10.28	100.0	25	30	-7.0	78.0	0.860	0.431	6.9 %
D5000	5500	10.0	10.28	100.0	25	60	2.0	-7.0	0.950	0.368	6.7 %
D5000	5800	8.0	8.90	80.0	25	0	15.0	-59.0	0.964	0.358	6.7 %
D5000	5500	11.0	8.90	80.0	25	15	-38.0	-1.0	0.967	0.355	6.6 %
D5000	5200	10.0	10.28	100.0	25	60	-18.0	-16.0	0.964	0.355	6.6 %
D5000	5500	10.0	10.28	100.0	25	30	2.0	-23.0	0.942	0.364	6.3 %
D5000	5800	17.0	6.59	10.0	25	45	-44.0	57.0	1.001	0.325	6.3 %
D5000	5600	10.0	8.90	80.0	25	30	-20.0	-53.0	1.016	0.315	6.2 %
D5000	5600	10.0	10.28	100.0	25	15	3.0	-36.0	0.936	0.367	6.2 %
D5000	5600	10.0	10.28	100.0	25	30	14.0	-5.0	0.903	0.386	6.1 %
D5000	5500	10.0	10.28	100.0	25	30	4.0	-46.0	0.952	0.355	6.1 %
D5000	5500	10.0	8.90	80.0	25	30	-4.0	2.0	0.985	0.333	6.1 %
D5000	5600	10.0	8.91	40.0	25	30	-26.0	39.0	1.005	0.317	5.9 %
D5000	5500	10.0	8.90	80.0	25	30	-11.0	-13.0	0.996	0.322	5.9 %
D5000	5500	10.0	10.28	100.0	25	75	4.0	-63.0	0.928	0.362	5.7 %
D5000	5600	10.0	10.28	100.0	25	45	-8.0	-73.0	0.941	0.353	5.6 %
D5000	5500	17.0	5.67	20.0	25	45	10.0	-105.0	1.043	0.287	5.6 %
D5000	5200	10.0	8.90	80.0	25	15	-14.0	20.0	0.945	0.348	5.5 %
D5000	5600	10.0	8.91	40.0	25	30	-9.0	-23.0	1.024	0.297	5.5 %
D5000	5200	10.0	8.90	80.0	25	0	-14.0	-21.0	0.961	0.334	5.3 %
D5000	5200	10.0	8.90	80.0	25	30	-7.0	19.0	0.946	0.340	5.2 %
D5000	5600	10.0	8.90	80.0	25	45	12.0	-34.0	0.975	0.321	5.1 %

Table 2: **Identified critical configurations for the cSAR system with a probability above 5% to exceed the MPE.** *Model error* is the standard deviation of the GP model error; *Failure prob.* is the probability of exceeding the MPE. Strictly speaking, the MPE is only known after the measurement is performed (see Eq 1), but it was a priori and conservatively set to be one of {1.5, 1.6, 1.7} dB, based on previous measurements using similar test conditions. For example, for VPIFA 750 cases, an MPE of 1.7 dB was used. In Fig 15, the MPE was found to be 1.8 dB for the two VPIFA measurements. Consequently, *failure prob.* would be lower if MPE = 1.8 dB was used.

Measurement of critical cases:. The 44 identified critical cases in Table 2 were measured at LAB1. The results are shown in Fig 15. It is observed that all measurements agree with the target values within the MPE. Thus this cSAR3D flat phantom has passed all of the validation criteria, and is considered to be fully validated for measurement use. Note that this only validates the individual cSAR3D flat phantom and not the class of all cSAR3D flat phantoms, since measurement accuracy is dependent on manufacturing tolerances and calibration quality. Therefore, each phantom must be individually validated.

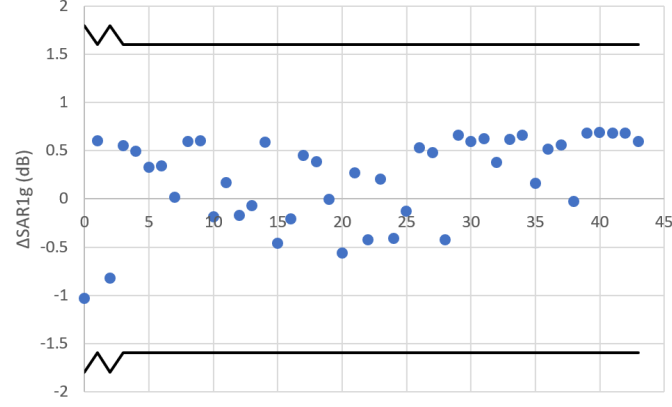


Figure 15: **Deviations of SAR_{1g} from numerical target values (ΔSAR_{1g}) measured on a cSAR3D flat phantom.** They are shown for the 44 critical configurations of Table 2, which were identified by the search algorithm as required additional measurement tests. All of the results are within the MPE limits (black lines), such that the measurement system passes the validation.

3.4. DASY8 Validation

The main differences in the obtained DASY8 results compared to cSAR3D stem from the fact that the deterministic component of the isotropic variogram is now very small compared to the nugget (see *Discussion*). The obtained isotropic semivariogram and good fit validation are summarized in Fig 16. As expected, given the small sill, the NRMSE is larger than in the cSAR3D case, but it is still comfortably within the 25% acceptance threshold. The residuals validation test results (see Fig 17) strongly contribute to confirming the GP model.

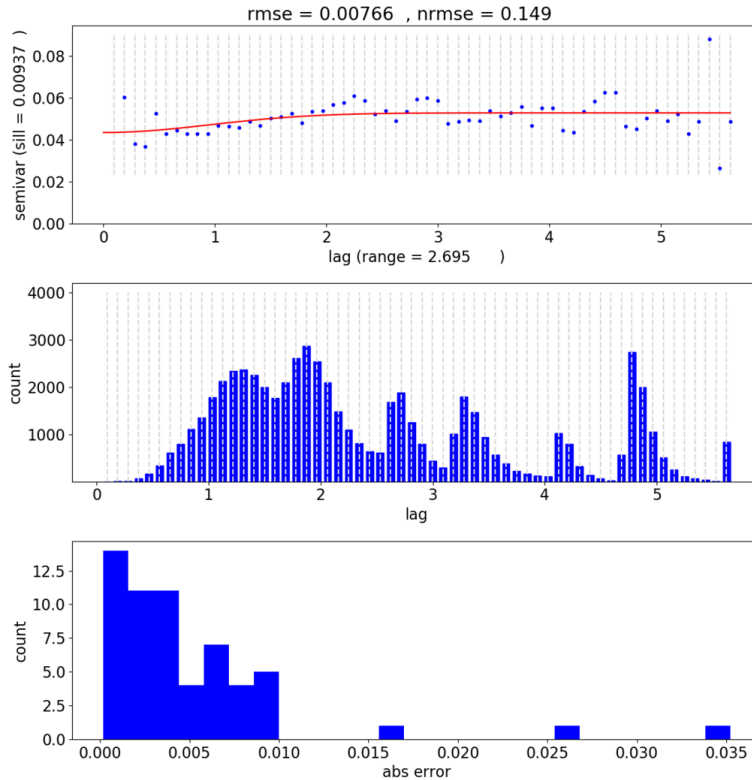


Figure 16: **Construction of the semivariogram for the DASY8 GP model.** The semivariogram is shown along with the histogram of the binned sample lags used for its construction and the histogram of the absolute errors between the empirical variogram and the fitted theoretical one. The validation of the fit quality returned an NRMSE of about 15%.

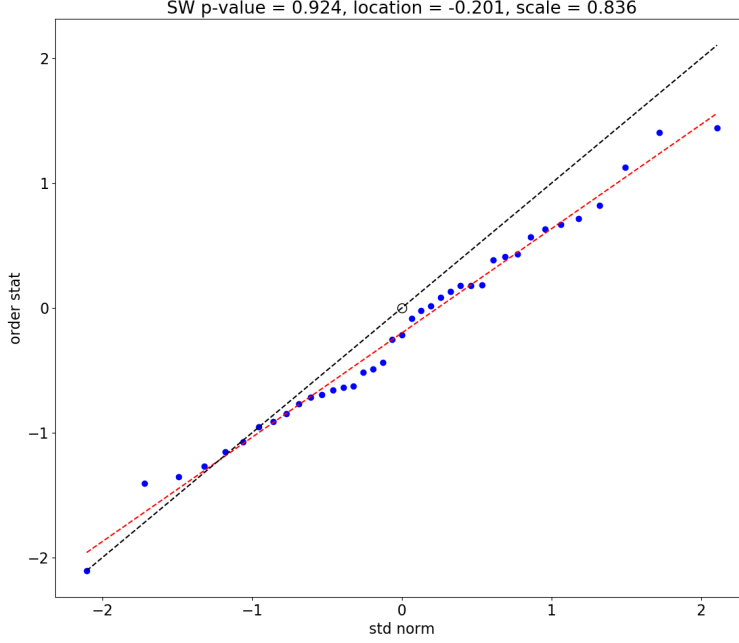


Figure 17: **Residuals QQ-plot of the DASY8 model confirmation step.** The Shapiro-Wilk test p-value, as well as the location and scale of the linear regression are well within their acceptance ranges, successfully confirming the GP model.

As a result of the prominent noise level, the Shapiro-Wilk test p-value is excellent. The slope of the QQ-plot regression is slightly below 1, which means that the model is on the conservative side (the estimated interpolation errors are in average slightly larger than those obtained through measurements), which pushes the search algorithm to use a larger initial sample and is likely to increase the validation effort.

In the DASY8 validation, no configuration with a failure probability above 5% of exceeding the MPE value was found, which did not come as a surprise, considering the precision of the system-under-validation. In other words, the critical search for failures was performed and no critical point was returned. Therefore, the evaluated DASY8 system (including specific probe and phantom used) is considered to be validated.

4. Discussion

4.1. Revealing Device-Specific Failure Risk Heterogeneity

When analyzing the search algorithm performance for the cSAR3D (x, y, θ) -subcube GP model using intentionally lowered – i.e., stricter – MPEs, clear clustering of the revealed configurations at risk of exceeding the MPE are evident in Fig 11 and 12. While they do not constitute a real danger of failing the validation (the MPE was artificially lowered to the point where failure predictions start appearing), the clustering around specific spatial locations and angular orientations reveal how a combination of sensor placement and field reconstruction methodology results in a heterogeneous distribution of the measurement error throughout the configuration space. Despite using a validation approach that is device agnostic, the GP model-based approach is capable of revealing such variations, and of assessing the probability of measurement errors exceeding the tolerances.

4.2. Behavior Comparison Between cSAR3D and DASY8

For the DASY8 system, the deterministic component of the isotropic variogram is almost negligible compared to the *nugget*, which results from thermal noise, amplifier instability, stochastic placement and other operator inaccuracies, etc. This means that the sill is significantly smaller and close to the nugget. The cSAR3D and DASY8 system nuggets have nearly the same magnitude, indicating that their noise levels are comparable. However, in the cSAR3D case, the sill is large compared to the nugget, indicating that systematic (i.e., reproducible) deviations from the reference value cannot be neglected compared to the measurement noise anymore. Importantly, the GP model approach performs

correctly in both situations and remains as effective in the presence of a high relative amount of noise as in the almost deterministic cases. This further strengthens the confidence in the general applicability of the developed validation approach.

The possibility of augmenting the GP model quality using manufacturer knowledge, without compromising the trustworthiness of the validation (thanks to the independently performed model confirmation step), could also be demonstrated for the DASY8 system.

4.3. Benefits of the developed methodologies

The developed validation approach offers a range of important and valuable features:

- Validation can readily be performed by an *independent party*; in fact, different parts of the validation can be performed by different parties, thus maximizing trust in the validation,
- It *maximizes the likelihood* of detecting potential configurations that violate the MPE limit,
- It incorporates *stochastic elements*, which ensures comprehensive coverage over time, avoids bias, and prevents preferential calibration for known validation benchmark configurations,
- It is a *device-agnostic* approach where no device-specific knowledge is assumed, such that is ideally suited for harmonizing the divergent standards of scanning- and array-based systems; at the same time, manufacturers are free to use their knowledge to reduce the GP model generation effort.

These benefits make the proposed approach also attractive for other applications beyond SAR measurement device validation.

The proposed validation method can be performed and repeated with a reasonable effort (one day of measurements) by a suitable test-lab or the device user. It has been demonstrated on two different scan systems and can be implemented in a simple software tool, such that it can easily be followed despite the complexity of the underlying mathematics.

Beyond the benefits for validation purposes, the developed methodologies also offer:

- an efficient approach for exploring high-dimensional parameter spaces with a very small training set that furthermore is generated in a non-iterative manner (important in the given application context, as a single measurement session is desired; this is, e.g., not the case for the sophisticated approaches from [35] or [6]);
- a search algorithm that exploits knowledge of the variogram at each iteration for increased computational efficiency; this implies the ability to use large search populations, with no need for elaborate initial designs based on refined models. Increasing the search population allows to detect even highly local anomalies.

The present approach addresses a need that is not typically covered in reliability theory (such as [1], [3], or [11]), as it permits the identification of a single outlier (detection of global extrema) that fails to satisfy the MPE, rather than the estimation of a probability of system failure, which might be close to zero (keyword: ‘measure theory’, ‘almost always true’). In consequence, the search algorithm is not a typical Design of Experiments approach; it can be interpreted as a heuristic global optimization algorithm with an uncertainty component that is simultaneously population and trajectory based. A simple, model-agnostic space-filling design (such as LHS) is sufficient to initiate the algorithm.

Comparison to Bayesian methods: A disadvantage of classical kriging compared to Bayesian methods is that it fails to incorporate uncertainty about the covariance (variogram) into its measure of interpolation error. This typically leads to overestimated confidence in the interpolated values. With the proposed approach, the application of the variogram RMSE into the resulting estimated error alleviates this problem. On the other hand, Bayesian hierarchical methods are computationally costlier and typically rely on known prior distributions or iterative approaches – both of which are excluded in our application. In addition, Bayesian methods are often increasingly slow as the number of dimensions increases, which the presented approach avoids.

Extensibility: The present approach can readily be extended in view of future evolutions of the measurement standards, e.g., by adapting to configuration space to include other frequencies, modulation schemes, or antennas.

4.4. Limitations

In this section, study limitations and potential generalizations of the proposed approach/methodology are discussed.

Assumptions:. The space is *geometrically anisotropic* and can be made isotropic through linear transformation; if that is not the case, nested model, multi-fidelity models, or multiple models valid in subspaces can be used. In addition, a *zero drift process* is assumed throughout the space (otherwise, universal kriging is needed). *Stationarity, monotonic semivariograms, separability and continuity* are assumed (see above). Various generalizations are possible at the cost of increased complexity, which includes, replacing ordinary kriging by universal kriging, geometric anisotropy by zonal anisotropy, and treating continuous domains with categorical variables.

Variability:. *Operator variability* is included in the noise and nugget, but is likely operator specific (operator error might anyway trigger remeasurement if outliers are apparent). *Poor device consistency* (manufacturing or calibration) will result in failure of confirmation step that could be remedied by creating a specific GP model for that device.

Measurement efficiency:. The LHS nature of S makes the measurement process slow as each sample point requires a completely different measurement configuration. In practice, shortcuts might be taken as long as one is confident enough about the resulting values.

Other application-related aspects:. The current study focuses on *flat phantoms* and still needs to be applied to the slightly more complicated situation in head phantoms, where the lack of translational symmetry increases the configuration space. There are *other aspects of system validation* that are taken care of outside the GP model of this paper. Simultaneous transmission of multiple signals (as done using 5G signals with carrier aggregation to improve bandwidth, for example) is validated separately. Another example is the validation of dynamic power control systems of mobile phones, where the signal amplitude is adjusted over time to keep the SAR below the regulatory limit.

Surrogate modeling approach:. GP modeling is a vast field in which more sophisticated approaches than the ones employed here exist for model construction, validation, and exploitation. For instance, it might be preferable to use maximum likelihood or cross-validation to select the covariance parameters, or the negative log predictive density (NLPD) could complement the RMSE in the quality assessment. In fact, other non-GP surrogate modeling approaches could be employed, as long as they are capable of providing conservative variance estimates (the validation step will need to be adapted if ordinary kriging is not used). However, in view of the purpose of this study – namely identifying a practical solution to the specific problem of SAR system validation and to the more general one of efficiently and reliably validating systems with a large configuration space in an unbiased, implementation-agnostic and independently verifiable manner – choices were dictated by the benefits listed above, as well as the simplicity and ready availability of suitable routines, and are justified by the successful application.

5. Conclusion

A general, robust, trustworthy, efficient, and comprehensive validation approach has been developed that can operate agnostically of the technical implementation of the tested device, prevents calibration that favors known validation benchmarks, and is applicable to large configuration spaces. Its application, suitability, and strength has been demonstrated through rigorous validation of two technically completely different SAR measurement systems, i.e., a scanning system and an array system, and involved two different laboratories for separate steps in the process to illustrate how the approach permits independent verification of the validation.

The proposed SAR system validation resolves the current problem of unifying and demonstrating equivalence of the IEC standards [15] and [16]. At the same time, it establishes a process by which any laboratory or user can prove at any time and with reasonable effort (less than one day) that a specific unit meets the required confidence interval of $\pm 30\%$ for SAR evaluations, using an extended set of the already defined and currently available validation sources.

The proposed validation approach is general (i.e., not specific to the SAR measurement system) and can be made available as a simple software tool, such that it can easily be followed despite the complexity of the underlying mathematics. Overall the procedure will improve the quality, reliability, and reproducibility of the assessment of wireless devices conformity with safety regulations which benefits the public, government agencies and industry alike.

6. Acknowledgment

This research was partially supported by SEAWave (EU HORIZON-HLTH-2021-ENVHLTH-02, Grant Agreement-101057622). We thank our colleagues Profs. Luc Martens, and Theodore Samaras for their invaluable inputs, Nitin Jain for performing the SAR measurements at the BNN lab. and Sabine Regel for careful review of the manuscript. We specially thank Tim Harrington (FCC, USA) and Gréguy Saint-Pierre (ISED, CA) for providing the perspectives of the regulators.

7. Conflicts of Interest

Niels Kuster is co-founder, co-owner, and board president of SPEAG, which manufactures SAR measurement equipment. Mark Douglas is partly employed by SPEAG.

8. Supporting Information

8.1. Background and Theory on GP modeling

This section describes the theory needed to define geometric GP models, to build them from finite sets of known values, and to use them to perform spatial inference on the underlying data space. The background theory is well known: it was first established in the field of geostatistics by [23] and detailed accounts can be found in the literature (e.g., [19] or [9]). Note that in geostatistics, the configuration spaces are typically 2–3 dimensional, while here a higher dimensional space is being applied (see the Supporting Information).

A *Gaussian process* is a stochastic process $Y = \{Y(x) : x \in X\}$ of random variables $Y(x) = Y_x : X \rightarrow \mathbb{R}$ over a convex connected index set $X \subset \mathbb{R}^n$ such that for every finite subset $\{x_1, \dots, x_k\}$ of elements of X , the tuple $Y_{x_1, \dots, x_k} = (Y_{x_1}, \dots, Y_{x_k})$ is a multivariate Gaussian random variable, or equivalently such that every linear combination $\sum_{i=1}^k w_i Y_{x_i}$ follows a univariate normal distribution. The index set X is the underlying *domain* or *parameter space*. In general, a stochastic process is *separable* on X if it is uniquely determined from a countable set of points (such as $X \cap \mathbb{Q}^n$). Moreover, a process is said to be (*sample*) *continuous* if almost all its realizations are continuous. More generally, a process is *weakly continuous* if it can be decomposed as a sum of a continuous process and an uncorrelated noise component. All Gaussian processes will be assumed to be separably weakly continuous.

The Gaussian process $\{Y(x)\}$ is completely characterized by a mean function $\mu(x) = \mathbb{E}[Y(x)]$ and a positive definite covariance function $C(x_1, x_2) = \text{Cov}(Y(x_1), Y(x_2))$, so that it is strict-sense stationary if and only if it is wide-sense stationary:

$$\mu(x_1) = \mu(x_1 + x_2), \quad C(x_1, x_2) = C(x_1 - x_2, 0), \quad \mathbb{E}[|Y(x_1)|^2] < \infty,$$

for all x_1, x_2 in X . From now on Y will always be assumed to be *stationary*: such a process has a constant mean and on two points x_1, x_2 only depends on the difference $h = x_2 - x_1 \in \mathbb{R}^n$, as opposed to the actual positions of these two points in X . If the process only depends on the euclidean distance $|h|$, it is said to be *isotropic*, otherwise it is *anisotropic*. The process is *geometric* if there exists an invertible linear map $\iota : X \rightarrow \iota(X)$ in $GL_n(\mathbb{R})$ such that the process $Y_\iota = Y \circ \iota^{-1}$ on $\iota(X)$ is isotropic. Clearly, an isotropic process is geometric.

The *semivariogram* $\gamma : \mathbb{R}^{2n} \rightarrow \mathbb{R}$ can be defined through the relation

$$2\gamma(x_1, x_2) = \text{Var}(Y(x_1) - Y(x_2)), \quad (6)$$

where in the stationary case γ is also defined as a univariate function $\gamma : \mathbb{R}^n \rightarrow \mathbb{R}$ by $\gamma(h) = \gamma(0, h)$ via the relation $\gamma(x_1, x_2) = \gamma(x_2 - x_1)$. The corresponding *variogram* is 2γ . If the process is furthermore isotropic, then γ can be defined on \mathbb{R} by $\gamma(|h|) = \gamma(h)$, in which case γ is called *isotropic*. More generally for a subvector space V of \mathbb{R}^n , a semivariogram γ is said to be *directional* on X along V if γ is isotropic on $X \cap V$. Obviously, an isotropic semivariogram is directional, and any directional semivariogram γ can be defined on \mathbb{R} by setting $\gamma(|h|) = \gamma(h)$. From now on γ is assumed to be monotonic on $|h|$ and to be directional on some subspace of X . Fig 1 depicts a stationary, isotropic variogram and its characteristics, the nugget, sill and range, as described below.

As the expectation of a square, $\gamma(x_1, x_2) \geq 0$ for all x_1, x_2 . At lag $h = 0$, $\gamma(0) = \gamma(x, x) = \mathbb{E}[(Y(x) - Y(x))^2] = 0$, such that γ is always zero at the origin. Nevertheless, the limit

$$n_\gamma = \lim_{h \rightarrow 0} \gamma(h)$$

can be non-zero and is called the *nugget*. When $n_\gamma > 0$, it describes the height of the discontinuous jump at the origin. In case X has no spatial dependence the variogram is the constant $\text{Var}(Y(x))$ everywhere except at the origin, where it is zero. As explained in [9] paragraph 2.3.1 it can be shown that a stationary separable Gaussian process is continuous if and only if it is *mean square continuous* in the sense that

$$\lim_{|h| \rightarrow 0} \mathbb{E}[|Y(x+h) - Y(x)|^2] = 0 \quad \text{for all } x \in X,$$

and this is true if and only if $n_\gamma = 0$. When $n_\gamma \neq 0$ it is still assumed that Y is weakly continuous, so that the origin is the only point of discontinuity in the variogram.

In the directional case, the limit

$$s_\gamma = \lim_{|h| \rightarrow \infty} \gamma(h)$$

exists and is called the *sill* of the semivariogram γ . The lag r_γ at which $s_\gamma - \gamma(h)$ becomes negligible is called the *range*: when $s_\gamma = \gamma(h)$ for some h , then r_γ is the infimum of all such h ; while for models with an asymptotic sill, r_γ is conventionally taken to be the distance at which the semivariance first reaches 95% of the sill.

Since in practice it is impossible to sample everywhere, the interval $[0, \infty)$ is binned and for a finite set of known sample $S = \{y_i\}$, the function γ is estimated based on the empirical variogram $\hat{\gamma}$ defined by

$$\hat{\gamma}(h) := \frac{1}{2N(B_h)} \sum_{|y_i - y_j| \in B_h} (y_i - y_j)^2, \quad (7)$$

for B_h the bin that contains h and $N(B_h)$ the cardinality of the set $\{|y_i - y_j| \in B_h\}$; this estimator is also referred to as the *Matheron semivariance estimator*. Of course the binning, the size and evenness of the sample all play major roles in the quality of the resulting $\hat{\gamma}$. A theoretical variogram model is then fit to the empirical values – we say that γ *fits* Y on S . Three of the most common models and their inverses are given below:

- The *Exponential* model and its inverse have the form

$$\gamma(h) = n_\gamma + s_\gamma \left(1 - e^{-\frac{3h}{r_\gamma}}\right) \quad \text{and} \quad \gamma^{-1}(g) = -\frac{r_\gamma}{3} \log \left(1 - \frac{g - n_\gamma}{s_\gamma}\right). \quad (8)$$

- The *Gaussian* model and its inverse have the form

$$\gamma(h) = n_\gamma + s_\gamma \left(1 - e^{-\frac{4h^2}{r_\gamma^2}}\right) \quad \text{and} \quad \gamma^{-1}(g) = \frac{r_\gamma}{2} \left(-\log \left(1 - \frac{g - n_\gamma}{s_\gamma}\right)\right)^{\frac{1}{2}}. \quad (9)$$

- The *Spherical* model and its inverse have the form

$$\gamma(h) = n_\gamma + \frac{s_\gamma}{2r_\gamma} (3h - h^3) \quad \text{and} \quad \gamma^{-1}(g) = P \left(\frac{2r_\gamma}{s_\gamma} (g - n_\gamma) \right), \quad (10)$$

where $P(X) \in \mathbb{R}[X]^*$ is the polynomial inverse to $3X - X^3$.

A *geometric GP model* is a commutative diagram

$$\begin{array}{ccccc} S & \xrightarrow{\text{inc}} & X \times \Omega & \xrightarrow[\cong]{\iota \times \text{id}} & \iota(X) \times \Omega \\ & \searrow y & \downarrow Y & \swarrow Y_\iota & \\ & & \mathbb{R} & & \end{array} \quad (11)$$

endowed with a monotonic isotropic semivariogram $\gamma : \mathbb{R}^+ \rightarrow \mathbb{R}^+$ that fits Y_ι on S , where:

- $S = \{x_i\}$ is a finite subset of $X \subset \mathbb{R}^n$;
- $Y = \{y : X \rightarrow \mathbb{R}\}$ is a geometric, separable, stationary, and weakly continuous Gaussian process with probability space Ω ;

- Y_ι is isotropic with ι an invertible linear map in $GL_n(\mathbb{R})$.

The commutativity of the diagram implies the process is fully known on S , with

$$Y(x_i, \omega) = y(x_i) =: y_i \quad \text{for all } x_i \in S, \omega \in \Omega, y \in Y.$$

Writing $\bar{S} = \{(x, Y(x)) : x \in S\} \subset \mathbb{R}^n \times \mathbb{R}$, a geometric GP model is characterized by the triple (\bar{S}, ι, γ) which can be used to fully represent the model in a software implementation. Under the geometric GP model assumptions, \bar{S} is sufficient to build a full model. The approach is as follows:

- 1) Given \bar{S} , one can build ι by probing spatial dependencies along all possible (1-dimensional) directions in the data space. Under the geometric assumption of a GP model an iso-variance contour forms an $(n-1)$ -dimensional ellipsoid in X . This ellipsoid can be mapped to an $(n-1)$ -sphere via a series of rotations and axis rescalings. The composition of these invertible linear maps on \mathbb{R}^n form $\iota : \mathbb{R}^n \rightarrow \mathbb{R}^n$ which can be represented as a matrix in the canonical base of the data space.
- 2) Given \bar{S} and ι , one can compute an empirical semivariogram $\hat{\gamma}$ on the isotropic space $\iota(X)$, on which a semivariogram γ can be fitted. Most often, the model and binning are set a priori, they depend on the application field, while the range, sill and nugget are the result of a fitting algorithm.

A GP model can then be used for spatial inference at any unobserved location $x \in X$. The approach given below is known as *ordinary kriging*. The unknown value $Y(x)$ and the estimator $\hat{Y}(x)$ are interpreted as random variables located at x . For known values $\{y_i = \hat{Y}(x_i) = Y(x_i)\}_{i=1}^k$, $Y(x)$ is estimated as a linear combination

$$\hat{Y}(x) = (w_1 \quad w_2 \quad \cdots \quad w_k) \cdot \begin{pmatrix} y_1 \\ y_2 \\ \vdots \\ y_k \end{pmatrix} = \sum_{i=1}^k w_i(x) y_i, \quad (12)$$

where the weights $\{w_i(x)\}_{i=1}^k$ satisfy

$$\sum_{i=1}^k w_i(x) = 1 \quad \text{and} \quad \begin{pmatrix} \gamma_\iota(x_1, x_1) & \cdots & \gamma_\iota(x_1, x_k) \\ \vdots & \ddots & \vdots \\ \gamma_\iota(x_n, x_1) & \cdots & \gamma_\iota(x_k, x_k) \end{pmatrix} \begin{pmatrix} w_1(x) \\ \vdots \\ w_k(x) \end{pmatrix} = \begin{pmatrix} \gamma_\iota(x_1, x) \\ \vdots \\ \gamma_\iota(x_k, x) \end{pmatrix}, \quad (13)$$

for $\gamma_\iota(x_i, x_j) = \gamma(|\iota(x_i) - \iota(x_j)|)$. The first condition is true if and only if the estimator is unbiased:

$$\sum_{i=1}^k w_i(x) = 1 \quad \Longleftrightarrow \quad \mathbb{E}[\hat{Y}(x) - Y(x)] = 0. \quad (14)$$

The second condition ensures that the estimator variance ('kriging error') is minimal; its value can be computed as

$$\begin{aligned} \sigma(x)^2 &:= \text{Var}(\hat{Y}(x) - Y(x)) \\ &= C_\iota(0) + \sum_{i,j} w_i(x) w_j(x) C_\iota(|x_i - x_j|) - 2 \sum_i w_i(x) C_\iota(|x_i - x|) \\ &= - \sum_{i,j} w_i(x) w_j(x) \gamma_\iota(x_i, x_j) + 2 \sum_i w_i(x) \gamma_\iota(x_i, x), \end{aligned} \quad (15)$$

where $C_\iota(h) := C(\iota(x), \iota(x+h))$ is the covariance function on the isotropic space $\iota(X)$ that satisfies $\gamma_\iota(h) + C_\iota(h) = C_\iota(0)$ for all h in \mathbb{R} . Finally, since by definition $\varepsilon(x) := \hat{Y}(x) - Y(x)$ is a linear combination of Gaussian random variables,

$$\frac{\varepsilon(x)}{\sigma(x)} = \frac{\hat{Y}(x) - Y(x)}{\sigma(x)} \sim \mathcal{N}(0, 1) \quad (16)$$

follows the standard normal distribution.

8.2. Delta Measure Derivation

Let $T \in \mathbb{R}$ be a fixed threshold and $\mathcal{M} = (\bar{S}, \iota, \gamma)$ a geometric GP model. For $\{Y(x) : X \rightarrow \mathbb{R}\}$ the underlying geometric Gaussian stationary process over $X \subset \mathbb{R}^n$ known on $S = \{x_i\}_{i=1}^k$, and for x_0 a point in X , a measure needs to be established of how far away from x_0 the next candidate point x must be to have a reasonably likelihood of $Y(x)$ *crossing* the threshold T in the sense that:

$$(Y(x) - T)(Y(x_0) - T) < 0.$$

The probability p that $Y(x) < T$ knowing that $y_0 = Y(x_0)$ for a neighboring point x_0 is

$$\begin{aligned} p &= P(Y(x) < T \mid Y(x_0) = y_0) \\ &= P(Y(x) - Y(x_0) < T - y_0 \mid Y(x_0) = y_0) \\ &= \Phi\left(\frac{T - y_0}{\sigma}\right), \end{aligned}$$

where σ^2 is the variance of the zero-mean Gaussian distributed variable $Y(x) - Y(x_0)$. In this case, the probability that $Y(x) > T$ knowing $y_0 = Y(x_0)$ is $1 - p$. Since by definition $\sigma^2 = 2\gamma$, assuming $p < \frac{1}{2}$,

$$\begin{aligned} \Phi\left(\frac{T - y_0}{\sigma}\right) &= p \\ \Leftrightarrow T - y_0 &= \sigma\Phi^{-1}(p) = \sqrt{2\gamma(h)}\Phi^{-1}(p) \\ \Leftrightarrow \gamma(h) &= \frac{1}{2}\left(\frac{T - y_0}{\Phi^{-1}(p)}\right)^2, \end{aligned}$$

for the lag $h = x - x_0 \in \mathbb{R}^n$. Along a given direction, γ is invertible on the interval $(0, r_\gamma]$ with $\gamma(r_\gamma) = s_\gamma$ for r_γ the range and s_γ the sill of γ . Then the continuous monotonic function can be defined $\delta_p : \mathbb{R}_+ \rightarrow \mathbb{R}_+$ as

$$\delta_p(l) = \begin{cases} 0 & \text{if } l \leq g_p(n_\gamma), \\ \gamma^{-1}\left(\frac{1}{2}\left(\frac{l}{\Phi^{-1}(p)}\right)^2\right) & \text{if } g_p(n_\gamma) < l < g_p(s_\gamma), \\ r_\gamma & \text{if } l \geq g_p(s_\gamma), \end{cases} \quad (17)$$

where

$$g_p(d) = \sqrt{2d}|\Phi^{-1}(p)|, \quad 0 < p < \frac{1}{2}, \quad (18)$$

for n_γ the nugget of γ . Knowing the values T and y_0 one can choose a parameter p and use $\delta_p(T - y_0)$ to find the closest points to x_0 with a probability $\geq p$ to cross the threshold T . The function δ_p , as illustrated in Fig 2, encodes all the covariance characteristics carried by the variogram:

- Parameter p is the probability that a realization $y(x)$ is on the other side of T ; it expresses the sensitivity of the model in the assessment of whether or not the true value $y(x)$ is considered to have crossed T . The smaller p (i.e., faster fluctuations are handled), the shorter the distance $h = |x - x_0|$ at which the system suspects T to potentially have been crossed, and hence the smaller $\delta_p(l)$ becomes. On the other hand, when p tends towards $\frac{1}{2}$, its most extreme value, the function δ_p reacts increasingly slowly to changes of h , up to the point where it no longer makes use of the information content of γ . More precisely, the variogram influences the predictions at a lag h if

$$\gamma(h) < s_\gamma \quad \Leftrightarrow \quad \frac{1}{2}\left(\frac{T - y_0}{\Phi^{-1}(p)}\right)^2 < s_\gamma \quad \Leftrightarrow \quad p < \Phi\left(-\frac{l}{\sqrt{2s_\gamma}}\right).$$

- Many models assume n_γ to be zero. However, when $|T - y_0|$ is smaller than a non negligible $g_p(n_\gamma) > 0$, the expected value of $Y(x)$ is so close to T that $\delta_p(l)$ is zero, which expresses the fact that it cannot be predicted on what side of T the true value $y(x)$ is likely to be.
- As y_0 approaches T , $\delta_p(l)$ approaches zero in accordance with γ .
- When $|T - y_0|$ is larger than $g_p(s_\gamma)$, x is too far away from x_0 for the condition $Y(x_0) = y_0$ to have an influence on the outcome of $Y(x)$.

8.3. Latin Hypercube Sampling

In order for the initial sample S to efficiently generate a GP model, in the sense that a minimal number of points is used to build a satisfactory model, sample S needs to be well spread over domain X . The choice made was to use *Latin Hypercube Sampling (LHS)* which is a type of stratified Monte Carlo sampling that generates a finite sample in an n -dimensional subset of \mathbb{R}^n isomorphic to the n -hypercube I^n . The method was first proposed in [24] and later on improved in [27] to minimize the integrated mean squared error and maximize entropy. For a sample of size k , I^n is partitioned such that the range of each dimension is partitioned into k equiprobable intervals. The resulting sample $S \subset I^n$ is such that:

- The projection of S on each dimension yields a distribution where each interval contains exactly one projected element;
- One value from each interval is selected at random with respect to the probability density in the interval.

Throughout this paper, all distributions undergoing LHS are uniform, so that I^n is divided into k^n equal n -dimensional *sub-cubes* ('cases'). It is further assumed that domain X has the form

$$X = \prod_{i=1}^n [\inf(X_i), \sup(X_i)], \quad (19)$$

where X_i denotes the interval of variable i , so as to make X isomorphic to I^n .

LHS Implementation:. For a unified LHS procedure to generate suitable sample sets for both the initial sampling (GP model construction) and the model testing, different conditions need to be satisfied. In addition, not all configurations in the configuration space X are valid (i.e., meaningful for the underlying of application). The following approach for generating a suitable LHS sample S of size k was employed:

- 1) A LHS sample S_0 of size k in $I^n = [0, 1]^n$ is generated so that:
 - I_n is partitioned into the canonical grid of k^n equally sized n -dimensional sub-cubes ('cases'). The elements of S_0 are placed in their own 'case', such that each row along each of the n dimensions contains exactly one element of S_0 , and that the minimal euclidean distance between two occupied squares is maximized,
 - each element of S_0 is placed within its 'case' according to a uniform probability distribution.

While the first condition guarantees a good initial sample, the second condition is essential for it to constitute an appropriate test sample.

- 2) Assuming X satisfies Eq 19, J_X is defined to be the continuous index domain

$$J_X = \prod_{i=1}^n J_i, \quad (20)$$

where

- $J_i = [\inf(X_i), \sup(X_i)]$ for continuously treated variables x , y , *angle*,
- $J_i = [\inf(X_i), \sup(X_i) + \frac{\sup(X_i) - \inf(X_i)}{k}]$ for discretely treated variables *frequency*, *par*, *bandwidth*, *distance*,
- $J_i = [0, 21]$ for the discrete index based variable *power*.

- 3) The set S_1 is defined as the image of S_0 via the obvious isomorphism $I \rightarrow J_X$.
- 4) The set $S \subset X$ is finally obtained from S_1 by snapping each coordinate of $x \in S_1$ to the closest meaningful value lower or equal to x . In the case of the power variable j this value is set to be $P_{\min}(x) + j$, for $P_{\min}(x)$ the minimal allowed power for x . Even though the power values are not exactly uniformly distributed over their domain interval, they are close enough to being uniform.

A custom LHS implementation based on pyDOE [2] was used, in order to have control over the seeds.

8.4. Size of Initial Search Population

How can it be ensured that S_0 is suitable for the initiation of algorithm 1? Including those cases where the likelihood of crossing T_-, T_+ is low (i.e., the T_* are far from the known values $Y(S_0)$), a method is needed to determine the sample size required for the search algorithm to either locate these out of bound elements, or – if none are found – to establish confidence that there are none.

Assume that $T_- < Y(x) < T_+$ for every x in S_* . For $x_0 \in S_*$ and $T \in \{T_-, T_+\}$, it is known by definition that for any continuous realization y of Y and for any $l = |y(x_0) - T|$, there is a $\delta > 0$ such that none of the elements in the open hyperball $B(x_0, \delta) \subset X$ of center x_0 and radius δ will cross T . Determining the supremum $\delta_{\sup}(y)$ of all these δ 's for each continuous y , and setting δ_{\inf} to be the infimum of all $\delta_{\sup}(y)$ would give a neighborhood around x_0 in which an element x is known not to cross one of the thresholds. The problem of course is that without further conditions on Y , a realization, even continuous, might be arbitrarily large in any given open neighborhood of x_0 , in other words $\delta_{\inf} = 0$. It is therefore impossible to guarantee with a finite sample in X and a finite searching algorithm that all out of bound elements will be found. However, the weakly continuous nature of the underlying process makes it possible to establish a condition with probability $0 < p < \frac{1}{2}$, in which δ_{\inf} reaches $\delta_p(l)$:

- For a finite sample $S_* \subset X$ in an isotropic space X with semivariogram γ , an element $x_0 \in S_*$ and a threshold $T_* \in \mathbb{R}$, the largest $\delta > 0$ such that the elements of $B(x_0, \delta)$ have a probability of at most p to cross T_* knowing γ is $\delta = \delta_p(|Y(x_0) - T_*|)$.

One can be confident, with probability $q = 1 - p$ for small $p > 0$, that all the points in the open subset of radius $\delta_p(l)$ around x_0 will not cross T . Ideally, the situation should be reevaluated by performing additional measurements at points in $x \in X$ that are distant by more than $\delta_p(l)$ from x_0 . In practice, because algorithm 1 searches along a single dimension at a time, it is sufficient to consider the $2 \cdot \dim(X)$ points on the hypersphere $S(x_0, \delta) = \partial B(x_0, \delta)$ that are located along directions $\{\vec{e}_i\}$.

The closer $y(x)$ is to T_* , the smaller δ becomes; therefore, for each $x \in S_*$ one is only interested in the threshold T that is the closest to $y(x)$. Assuming the values of S_* are evenly distributed over X , let

$$L_* = \{\min(|y(x) - T_-|, |y(x) - T_+|) : x \in S_*\}$$

and define \bar{l} to be the sample mean of L_* . Then, for X_i (the projection of X on its i th dimension; $1 \leq i \leq n = \dim(X)$) the positive integer

$$\nu_p = \prod_{i=1}^n \left\lceil \frac{\sup(X_i) - \inf(X_i)}{\delta_p(\bar{l})} \right\rceil \quad (21)$$

is suggested as an estimate of the required sample size. Here, ν_p is the number of points of the coarsest discretization of X resulting from uniform discretizations of all X_i with step interval at most $\delta_p(\bar{l})$. In practice, a uniformly distributed sample of size ν_p over X that incorporates a random element is desirable, such as a n -dimensional latin hypercube sample that maximizes the minimal distance between sample points. Clearly ν_p must and does increase with a higher required confidence $q = 1 - p$. As expected

$$\lim_{q \rightarrow 1} \nu_p = \lim_{p \rightarrow 0} \nu_p = \infty.$$

Note that, by definition $\delta_p(\bar{l}) \leq r_\gamma$, where r_γ is the range of γ . Isotropy ensures that r_γ is constant along all directions and is strictly less than $\max_i(\sup(X_i) - \inf(X_i))$, so that $\nu_p \geq 2$. It is also noteworthy that when $\mu(y(S_*)) = \frac{T_- + T_+}{2}$, the value \bar{l} is a measure of the dispersion of $y(S_*)$ around its mean $\mu = \mu(y(S_*))$ since in that case

$$\bar{l} = |T_* - \mu| - \text{mad}(y(S_*))$$

where

$$\text{mad}(y(S_*)) = \frac{1}{|S_*|} \sum_{x \in S_*} |y(x) - \mu|$$

is the mean absolute deviation of $y(S_*)$. Hence the more volatility there is in the distribution of $y(S_*)$ in the interval $[T_-, T_+]$, the smallest \bar{l} is and the largest ν_p becomes. While the volatility of $Y(s)$ is often expressed in terms of its standard deviation, the latter will fail, unlike \bar{l} , to take into consideration the closeness of T_* when $\mu(y(S_*)) \neq \frac{T_- + T_+}{2}$: in this case \bar{l} decreases as $\mu = \mu(y(S_*))$ approaches one of the thresholds. Even with low volatility of $y(S_*)$ around its mean, \bar{l} takes into consideration the increasing uncertainty regarding the crossing of one of the thresholds and ν_p will accordingly increase.

From the above, it follows that the proposed approach permits p to be set based on effort-reliability-balance considerations and ensures that the algorithm detects threshold violations with a user-defined sensitivity level.

8.5. Variables for System Validation of SAR Measurement Systems

8.5.1. Description of Scanning and Array Systems

The two commonly used SAR measurement systems are scanning systems (see Fig 18, left) and array systems (see Fig 18, right). Scanning systems use a robot to mechanically scan a single 3-axis E-field probe throughout the human phantom (e.g., head, torso or wrist phantom) [33]. Scanning systems are versatile in that the robot can, in principle, position the probe anywhere in the phantom with any measurement resolution. Therefore, the resolution-related measurement accuracy is not inherently limited by a fixed sensor spacing. A higher measurement resolution or a larger scanning volume results in longer scanning times, but irregular grids are commonly used to locally improve the resolution in regions around the SAR peaks. Direct SAR measurement approaches can in this way reduce the measurement uncertainty compared to fixed-grid array systems. The E-field probe of a scanning system is calibrated in well-controlled fields (e.g., using a waveguide filled with tissue-simulating liquid) [26], and the calibration uncertainty depends on the accuracy and stability of the instrumentation used (RF source, signal generator, amplifier, power meter, couplers, cables, etc.). The absolute positioning accuracy of the robot (i.e., shift in x or y position) does not significantly affect the measurement accuracy of the peak spatial-average SAR as long as the SAR peak is captured because the same probe is scanned over all measured locations.



Figure 18: **Two commonly used SAR measurement systems.** Target are scanned during the measurement of a mobile phone or other wireless device under test (DUT). The scanning system (left) phantom is filled with tissue-simulating liquid to allow for probe movement, and the DUT is positioned below. The array system (right) has no moving parts and therefore can be sealed. The DUT is placed on top of it.

Array systems use a large number of probes in a fixed grid to electronically scan the field in the phantom and are therefore much faster than scanning systems. However, array systems have additional measurement uncertainty contributions beyond those of scanning systems due to the fixed measurement grid and the large number of probes (hundreds to thousands) that must be calibrated individually. Mutual coupling between the probes limits how close the sensors can be to each other, which restricts the measurement resolution (however, multiple measurements with small device shifts can be used to improve the effective resolution for flat phantoms, but not for head phantoms or other curved phantoms due to the curvature-influence on exposure). The larger amount of material inside the phantom (probes, transmission lines, and supporting structure), compared to scanning systems, increases the scattering of the induced fields in the phantom. The scattering is affected by the field polarization and distribution, making it extremely difficult to fully characterise and remove during calibration. Scattering is also different at the boundaries of the array compared to the middle of the array. Due to field scattering, probes are typically restricted to a single plane conformal to the phantom surface and so cannot directly sample in the depth direction. This makes array systems dependent on field reconstruction algorithms to estimate the SAR at locations that cannot be measured.

8.5.2. Sources Used in the Validation

The source type determines the dominant field polarization and SAR pattern in the phantom. The three source types used in this study were chosen in accordance with IEC 62209-3 [16], where they are also described in detail. Dipole antennas (see Fig 19, left) are well suited for system validation as they can be designed for good impedance matching and a broad bandwidth in proximity to the phantom, and they give relatively high SAR values for a given input power level (resulting in inexpensive amplifiers capable of covering the dynamic range). The induced E-fields from a dipole antenna are predominantly polarized parallel to the phantom surface due to inductive coupling of the fields with the phantom [21]. 15 dipole antennas have been selected to cover the frequency range from 300 MHz to 6 GHz, including the most commonly used wireless device frequency bands. Individual dipoles are used at 300, 450, 750, 835, 900, 1450, 1750, 1950, 2300, 2450, 2600, 3700, 4200, and 4600, and one 5 GHz dipole covers 5200, 5500, 5600, and 5800 MHz. Validation dipoles have been selected in IEC 62209-3 for their good impedance match at a distance of $s = 10$ mm or 15 mm between the antenna feed point and the boundary between the phantom shell and the tissue-equivalent medium. This distance can be reduced to 5 mm or increased to 25 mm to modify the SAR pattern (and thereby test a larger range of SAR patterns) while keeping a good impedance match. At 300 MHz, 450 MHz, and 750 MHz, the 5 mm distance is excluded because it cannot be achieved due to the thicker dipole arms.

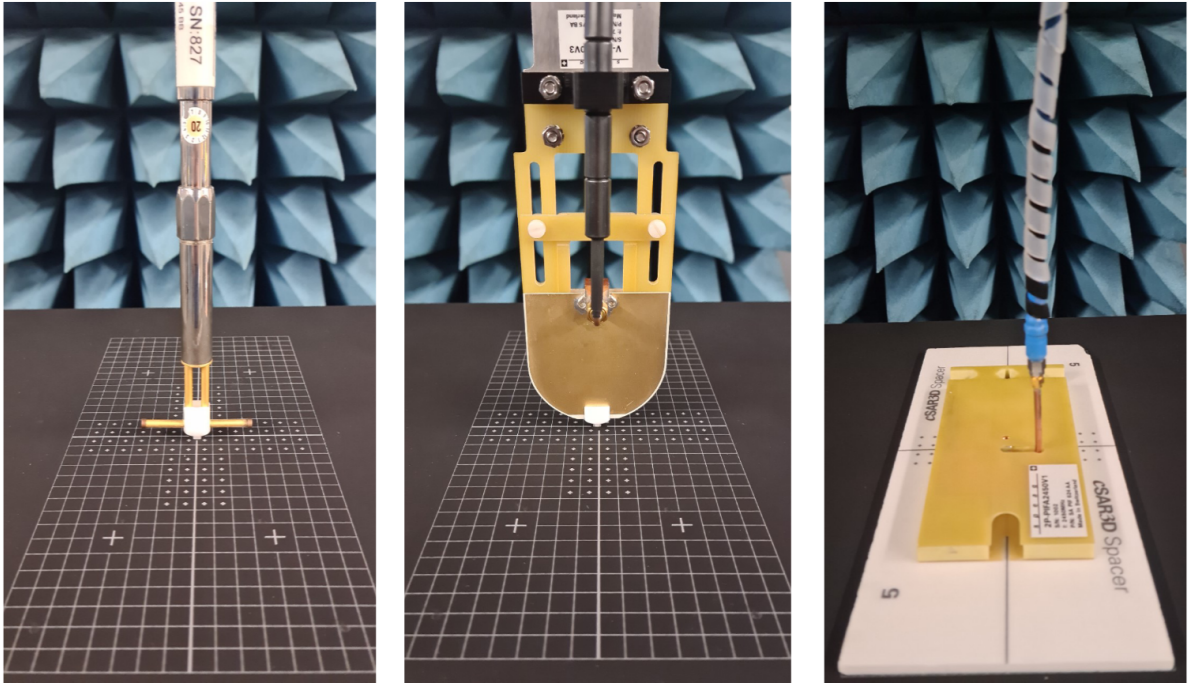


Figure 19: The dipole (left), VPIFA (middle), and CPIFA (right) sources mounted on a SAR array system.

Additional source types are needed to test other SAR patterns and polarizations. The VPIFA has been designed for IEC 62209-3 to address this condition [16]. It is also common to find SAR patterns from wireless devices with multiple SAR peaks, and so the dual-peak Centrally-fed Planar Inverted F Antenna (CPIFA) has been designed to address this.

The VPIFA (see Fig 19, middle) provides capacitive coupling to the phantom resulting in induced fields predominantly normal to the phantom surface. These evanescent fields decay rapidly, resulting in a sharp SAR distribution and thus providing a good test of the capability of the measurement system. Due to the localized field distribution, this source is well suited to be used on both flat and curved phantoms. A PIFA structure [31] is oriented such that the open end is close to the phantom and the short-circuited end is on the opposite end away from the phantom. To achieve capacitive coupling, the tip of the spacer of the VPIFA should be placed against the phantom outer surface, giving a distance of $s = 2$ mm to the phantom inner surface (the shell thickness is 2 mm). Larger distances are not used in order to preserve the capacitive coupling.

The CPIFA (see Fig 19, right) induces two SAR peaks in the phantom to test the ability of the

reconstruction algorithm to distinguish two peaks. The radiating structure of the CPIFA is also a planar-inverted F-antenna but with the open radiating end in two branches forming a T-shape. The two branches are modified by bending the open ends toward the phantom but using different lengths so that the two SAR peaks in the phantom have different values with a constant ratio. The CPIFA is oriented parallel to the phantom. A flat spacer with 5 mm thickness is used between the CPIFA and the outer surface of the flat phantom for antenna matching, giving a total distance of $s = 7$ mm to the phantom inner surface. Other distances are not used in order to maintain the ratio of the two SAR peaks.

8.5.3. Parameters of the Validation

This section motivates the selection of the following validation parameters: rotation angle θ , source location (x, y) , input power P_{in} , signal bandwidth BW and peak-to-average power ratio PAR . The frequency f and distance s parameters have been discussed in the previous section.

The rotation angle, θ , can be varied to create more SAR patterns and to test the isotropy of the probe to different tangential polarizations. All sources can be rotated at any angle from $\theta = 0^\circ$ to $\theta = 360^\circ$, and a fixed subset was chosen with angles that are an integer multiple of $\Delta\theta = 15^\circ$. An angular resolution of 15° gives a large number of samples and is easy for an operator to rotate by hand on the phantom with the aid of a protractor.

The accuracy of an array system may be sensitive to the devices location relative to the probes for three reasons. Firstly, current array systems have a relatively coarse resolution compared to the scan resolution of scanning system. Secondly, each individual probe in the array can be miscalibrated or malfunctioning. Thirdly, the reconstruction algorithm can be sensitive to location (e.g., due to the handling of measurement domain boundaries). It is therefore important to validate at all possible source locations (x, y) on the surface of the phantom. The physical boundaries of the array are marked on the phantom, and the validation region is defined as the physical boundary minus half of the SAR averaging cube on each side so that the cube edges are within the physical boundaries while the cube center is at the SAR peak. For the dipole antennas and VPIFAs, whose SAR peak location corresponds to the geometric center of the source, these locations refer to the center of the source. For the CPIFA, the center point (x, y) needs to be shifted to the location $(x - (a_i \cos\theta - b_i \sin\theta), y - (a_i \sin\theta + b_i \cos\theta))$, where a_i and b_i are the distances from the center of the source to the i^{th} SAR peak ($i = 1$ or 2) and θ is the rotation angle described previously.

The source is excited by a signal that has an input power level (P_{in}) and a modulation. A set of 24 modulations has been chosen for the study that representatively cover 3G, 4G, 5G, and WLAN signals used by wireless devices. An example 4G signal is shown in Fig 20. An unmodulated carrier (continuous wave signal, or CW) has been included to test the upper end of the dynamic range and a pulsed CW signal with a 10 ms period and 10% duty cycle has been included to test pure pulsed signals. The modulations were selected to provide the full range of PAR values (0 – 12 dB) and bandwidths (0 – 100 MHz) as shown in Table 3. These signals also differ in other parameters such as the modulation scheme (e.g., QPSK, 16-QAM [13]), the number of resource blocks (RB), and the multiple-access scheme (e.g., SC-FDMA [4], CP-OFDM [37]). These parameters do not directly affect the signal shape in the time-domain or frequency-domain, and therefore are not of primary importance to this study.

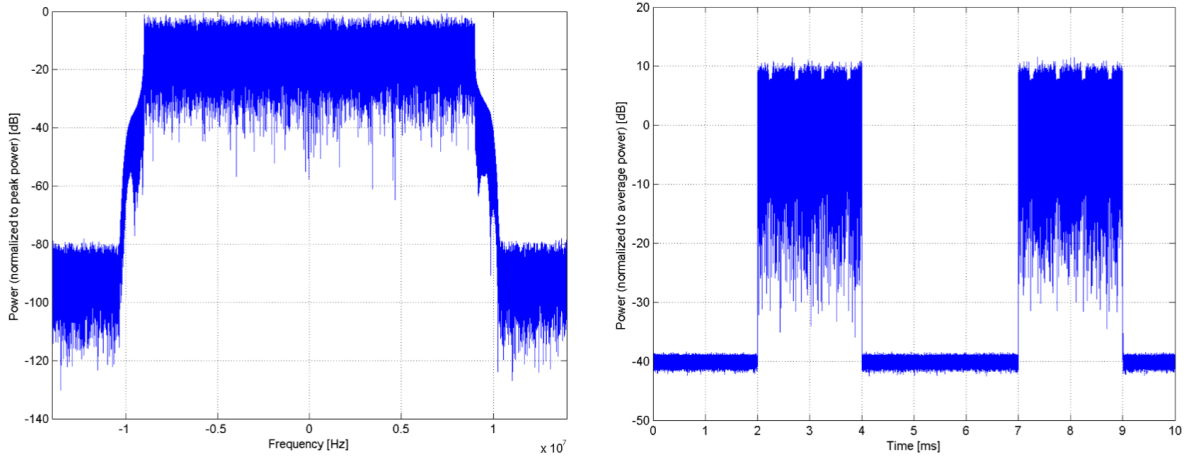


Figure 20: **Frequency (left) and time domain (right) plots of a 4th-generation (4G) cellular network signal.** Signal type: long-term evolution time domain duplex (LTE-TDD), single-carrier frequency domain multiple access (SC-FDMA), all resource blocks, quadrature phase shift keying (QPSK) modulation, with a 20 MHz bandwidth.

No.	Description	Type	PAR (dB)	BW (MHz)
1	Unmodulated carrier	CW	0	0
2	Pulse signal with a period of 10 ms and a duty cycle of 10 %	pulsed	10	0
3	WCDMA, 12.2 kbps RMC, IS-2000	3G	2.91	5
4	UMTS-FDD (HSDPA)	3G	3.98	5
5	LTE-TDD (SC-FDMA, 1 RB, 20 MHz, QPSK, UL Subframe=2,7)	4G	11.96	0.2
6	LTE-FDD (SC-FDMA, 100% RB, 1.4 MHz, QPSK)	4G	5.76	1.4
7	LTE-FDD (SC-FDMA, 100% RB, 1.4 MHz, 16-QAM)	4G	6.41	1.4
8	LTE-TDD (SC-FDMA, 1 RB, 1.4 MHz, 64-QAM)	4G	10.26	1.4
9	LTE-FDD (SC-FDMA, 100% RB, 3 MHz, QPSK)	4G	5.73	3
10	LTE-FDD (SC-FDMA, 100% RB, 3 MHz, 64-QAM)	4G	6.65	3
11	LTE-FDD (SC-FDMA, 100% RB, 5 MHz, QPSK)	4G	5.75	5
12	LTE-FDD (SC-FDMA, 100% RB, 5 MHz, 16-QAM)	4G	6.44	5
13	LTE-FDD (SC-FDMA, 100% RB, 10 MHz, 64-QAM)	4G	6.59	10
14	LTE-FDD (SC-FDMA, 100% RB, 20 MHz, QPSK)	4G	5.67	20
15	5G NR (DFT-s-OFDM, 1 RB, 50 MHz, QPSK, 30 kHz)	5G	5.68	0.4
16	5G NR (CP-OFDM, 1 RB, 80 MHz, QPSK, 30 kHz)	5G	7.89	0.4
17	5G NR (CP-OFDM, 1 RB, 100 MHz, QPSK, 30 kHz)	5G	7.93	0.4
18	5G NR (CP-OFDM, 1 RB, 40 MHz, QPSK, 60 kHz)	5G	7.7	0.8
19	5G NR (CP-OFDM, 50% RB, 50 MHz, QPSK, 15 kHz)	5G	8.43	25
20	5G NR TDD (CP-OFDM, 100% RB, 100 MHz, 256-QAM, 30 kHz)	5G	10.28	100
21	IEEE 802.11a/h WiFi 5 GHz (OFDM, 24 Mbps)	WLAN	9.38	20
22	IEEE 802.11a/h WiFi 5 GHz (OFDM, 36 Mbps)	WLAN	10.12	20
23	IEEE 802.11ax (40MHz, MCS1, 90pc duty cycle)	WLAN	8.91	40
24	IEEE 802.11ax (80MHz, MCS5, 90pc duty cycle)	WLAN	8.9	80

Table 3: **The 24 signal types selected for this study.** Signal 5 is shown in Fig 20.

The input power is set to give a certain target SAR value. The dynamic range of the SAR measurement system needs to be covered, which typically ranges from 0.1 W/kg to 100 W/kg for the peak SAR level. Reliability should be tested up to an upper bound of 100 W/kg for the local SAR, which corresponds to the extremity 10 g-averaged SAR limit of 4 W/kg for any modulated signal. To cover the dynamic range, a fixed 20 dB range of power levels has been chosen for all signals. The 20 dB range gives SAR values from 1 – 100 W/kg for the unmodulated (CW) signal and from 0.1 – 10 W/kg for all modulated signals. The actual input power levels depend on the source type, frequency and distance. These are shown in Table 4 for dipole antennas and Table 5 for the VPIFAs and CPIFA.

antenna name	f (MHz)	$P_{in,min}$ (dBm) at distance s			
		5 mm	10 mm	15 mm	25 mm
D300	300	–	–	16	17
D450	450	–	–	14	15
D750	750	–	–	11	13
D835	835	10	–	10	13
D900	900	9	–	10	12
D1450	1450	5	6	–	12
D1750	1750	4	5	–	12
D1950	1950	2	4	–	12
D2300	2300	1	3	–	12
D2450	2450	0	3	–	12
D2600	2600	0	3	–	12
D3700	3700	-2	2	–	12
D4200	4200	-3	2	–	12
D4600	4600	-3	2	–	11
D5000	5200	-4	2	–	10
D5000	5500	-5	1	–	10
D5000	5600	-4	1	–	10
D5000	5800	-4	1	–	8

Table 4: **Minimal input power $P_{in,min}$ for all dipole antennas and distances s to the phantom ensuring a SAR_{1g} of at least 0.1 W/kg.** The distance of $s = 5$ mm is not used for dipoles D300, D450, and D750 because the thicker dipole radius of 3.2 mm (as per requirements in [15]) does not allow this 5 mm distance (i.e., 3 mm distance to the phantom outer surface). The other dipoles have a radius of 1.8 mm.

antenna name	f (MHz)	s (mm)	$P_{in,min}$ (dBm)
V750	750	2	9
V835	835	2	9
V1950	1950	2	11
V3700	3700	2	11
C2450	2450	7	12

Table 5: **Minimal input power $P_{in,min}$ ensuring a SAR_{1g} of at least 0.1 W/kg for all VPIFAs and the CPIFA at the distance s to the phantom.**

8.6. Code Availability

A software implementation of the procedure is available at [5]:
<https://github.com/ITISFoundation/publication-IEC62209>

9. Abbreviations and Parameters

BW	bandwidth
GP	(geometric) Gaussian process
GL_n	general linear group of degree n
LHS	latin hypercube sampling
MAE	mean absolute error
MPE	maximal permissible error
NRMSE	normalized root mean square error
PAR	peak to average ratio
QQ	quantile-to-quantile
RMSE	root mean square error
SAR	specific absorption rate
SAR_{1g}	1g-averaged SAR
SW	Shapiro-Wilk test

B_h	the bin containing lag h
C	covariance function
e	error term
f	deterministic function; frequency
h	lag between two elements of X
I^n	unit n -cube
l	lag to threshold
m	number of iterations in Algorithm 1
n	dimension of X
n_γ	nugget of γ
$\mathcal{N}(\mu, \sigma^2)$	normal distribution with mean μ and standard deviation σ
p	sensitivity
P	probability measure on Ω
P_{in}	input power
q	repulsive force in algorithm 1
r_γ	range of γ
s	distance to phantom
s_γ	sill of γ
S	initial sample in X
S_i	sample at iteration i of the search algorithm
S_*	an element of $\{S_i : i \in \mathbb{N}\}$
\bar{S}	initial sample S with known values
T	test sample in X
T_\pm	thresholds in \mathbb{R}
T_*	an element of $\{T_-, T_+\}$
\bar{T}	test sample T with known values
w_i	kriging weights
x	element of X , first coordinate on array system
X	convex connected domain in \mathbb{R}^n
y	realization of Y , second coordinate on array system
Y	Gaussian process over X
Y_ι	isotropic process over $\iota(X)$
\hat{Y}	estimator of Y
α	pass criterion for variogram fit validation
γ	(theoretical) semivariogram
$\hat{\gamma}$	empirical semivariogram
δ_p	delta p -measure
θ	rotation angle
ι	linear isomorphism of X to its isotropic counterpart
μ	mean function
ν_p	search algorithm initial sample size
Φ	normal cumulative density function
Σ	matrix associated to ι
σ	standard deviation
Ω	set of outcomes in the underlying probability space

References

- [1] Azzimonti, D., et al. Adaptive design of experiments for conservative estimation of excursion sets. *Technometrics* 63.1: 13-26. 2021
- [2] Baudin M, Christopoulou M, Colette Y, Martinez, JM. pyDOE: The experimental design package for python. Available at <https://pythonhosted.org/pyDOE/#credits>.
- [3] Bect, J, Ginsbourger, D, Li, L, Picheny, V, Vazquez, E. Sequential design of computer experiments for the estimation of a probability of failure. *Statistics and Computing*, 22(3), 773-793. 2012.

- [4] Berardinelli G, Ruiz de Temino LAM, Frattasi S, Rahman MI, Mogensen P. OFDMA vs. SC-FDMA: performance comparison in local area int-a scenarios. *IEEE Wireless Communications*. 2008;15(5):64–72.
- [5] Bujard C, Neufeld E, Douglas M, Wiart J, Kuster N. A Gaussian-process-model-based approach for robust, independent, and implementation-agnostic validation of complex multi-variable measurement systems: application to SAR measurement systems [Computer software]. <https://github.com/ITISFoundation/publication-IEC62209>
- [6] Busby, D. Hierarchical adaptive experimental design for Gaussian process emulators. *Reliability Engineering & System Safety*, Vol. 94(7), 2009.
- [7] European Committee for Electrotechnical Standardization. CENELEC EN 50360 – Product standard to demonstrate the compliance of wireless communication devices, with the basic restrictions and exposure limit values related to human exposure to electromagnetic fields in the frequency range from 300 MHz to 6 GHz: devices used next to the ear. Brussels, Belgium, 2017.
- [8] European Committee for Electrotechnical Standardization. CENELEC EN 50566 – Product standard to demonstrate the compliance of wireless communication devices with the basic restrictions and exposure limit values related to human exposure to electromagnetic fields in the frequency range from 30 MHz to 6 GHz: hand-held and body mounted devices in close proximity to the human body. Brussels, Belgium, 2017.
- [9] Chilès, J-P, Delfiner, P. *Geostatistics: Modeling Spatial Uncertainty*, Second Edition. Wiley Series in Probability and Statistics. 2012.
- [10] Douglas MG, Kuster N. Novel fast SAR methods for compliance testing of wireless devices. *International Symposium on Electromagnetic Compatibility*, Tokyo. IEEE, 2014.
- [11] Dubourg, V, Sudret, B, Deheeger, F. Metamodel-based importance sampling for structural reliability analysis. *Probabilistic Engineering Mechanics*, 33, 47-57. 2013.
- [12] Council of the European Union. 1999/519/EC: Council Recommendation of 12 July 1999 on the limitation of exposure of the general public to electromagnetic fields (0 Hz to 300 GHz). 1999 Jul; 199:59-70, <http://data.europa.eu/eli/reco/1999/519/oj>.
- [13] Geyer JC, Doerr C, Aydinlik M, Nadarajah N, Caballero A, Rasmussen C, Mikkelsen B. Practical implementation of higher order modulation beyond 16-QAM. *Optical Fiber Communications Conference and Exhibition (OFC)*. 2015.
- [14] International Commission on Non-Ionizing Radiation Protection. Guidelines for limiting exposure to electromagnetic fields (100 kHz to 300 GHz). *Health Physics*, 2020;118(5):483–524.
- [15] IEC/IEEE 62209-1528. Measurement Procedure for the Assessment of Specific Absorption Rate of Human Exposure to Radio Frequency Fields From Hand-Held and Body-Worn Wireless Communication Devices—Human Models, Instrumentation and Procedures (Frequency Range of 4 MHz to 10 GHz). International Electrotechnical Commission Geneva, Switzerland, 2020.
- [16] International Electrotechnical Commission. IEC 62209-3 Measurement procedure for the assessment of specific absorption rate of human exposure to radio frequency fields from hand-held and body-mounted wireless communication devices – Part 3: Vector measurement-based systems (Frequency range of 600 MHz to 6 GHz). Geneva, Switzerland, 2019.
- [17] Innovation, Science and Economic Development Canada. Inter-laboratory fast SAR measurement campaign: overview of findings and recommendations. Report to IEC Project Team 62209-3, 2017.
- [18] IEEE. IEEE Std C95.1-1999 – IEEE Standard for Safety Levels with Respect to Human Exposure to Radio Frequency Electromagnetic Fields, 3 kHz to 300 GHz. Piscataway, NJ, USA, 1999.
- [19] Isaaks E, Srivastava RM. *An Introduction to Applied Geostatistics*. Oxford University Press, 1989, ISBN 0-19-505012-6.
- [20] Jawad, O, Lautru, D, Benlarbi-Delai, A, Dricot, J.M, De Doncker, P. Study of human exposure using kriging method. *Progress In Electromagnetics Research*, B(61), 241-252. 2014.

- [21] Kuster, N, Balzano Q. Energy Absorption Mechanism by Biological Bodies in the Near Field of Dipole Antennas above 300 MHz. *IEEE Transactions on Vehicular Technology*. 1992;41(1):17–23.
- [22] Mälicke M. SciKit-GStat 1.0: A SciPy flavoured geostatistical variogram estimation toolbox written in Python. *Geoscientific Model Development*. 2022; 15:2505–2532.
- [23] Matheron, G. Principles of geostatistics. *Economic Geology*. 1963;58:1246–1266.
- [24] McKay MD, Beckman RJ, Conover, WJ. A comparison of three methods for selecting values of input variables in the analysis of output from a computer code. *Technometrics*. American Statistical Association. 1979; 21(2):239–245.
- [25] Meier K, Burkhardt M, Schmid T, Kuster N. Broadband calibration of E-field probes in lossy media. *IEEE Transactions on Microwave Theory and Techniques*. 1996; 44(10):1954–1962.
- [26] Meyer R, Kühn S, Pokovic K, Bomholt F, Kuster, N. Novel Sensor Model Calibration Method for Resistively Loaded Diode Detectors. *IEEE Transactions on Electromagnetic Compatibility*. 2015;57(6):1345–1353.
- [27] Park JS. Optimal Latin-hypercube designs for computer experiments. *Journal of Statistical Planning and Inference*. 1994; 39(1):95–111.
- [28] Pokovic K, Nikoloski N, Christ A, Kuster N. Compliance Testing Tools and Procedures for Emerging Technologies (3-6 GHz). 18th International Conference on Applied Electromagnetics and Communications 2005 Oct 12 (pp. 1-4).
- [29] Pokovic K, Schmid T, Kuster N. Millimeter-resolution E-field probe for isotropic measurement in lossy media between 100 MHz and 20 GHz. *IEEE Transactions on Instrumentation and Measurement*. 2000 Aug;49(4):873-8.
- [30] Roustant O, Ginsbourger D, Deville Y. DiceKriging, DiceOptim: Two R packages for the analysis of computer experiments by kriging-based metamodeling and optimization. *Journal of statistical software*. 2012; 51:1–55
- [31] Sánchez-Hernández DA. Multiband integrated antennas for 4G terminals. Artech House. 2008.
- [32] Shapiro SS, Wilk MB. An analysis of variance test for normality (complete samples). *Biometrika*. 1965; 52(3-4):591—611.
- [33] Schmid T, Egger O, Kuster N. Automated E-field scanning system for dosimetric assessments. *IEEE Transactions on Microwave Theory and Techniques*. 1996;44(1):105–113.
- [34] Meyer R, Kühn S, Pokovic K, Bomholt F, Kuster N. Novel sensor model calibration method for resistively loaded diode detectors. *IEEE Transactions on Electromagnetic Compatibility*. 2015 Jul 24;57(6):1345-53.
- [35] Van Beers et al. Customized sequential designs for random simulation experiments: Kriging metamodeling and bootstrapping. *European journal of operational research* 186.3: 1099-1113. 2008.
- [36] Nagaoka, T, Wake K, Watanabe, S. Comparison of SARs measured by vector probe array-based SAR measurement systems using commercially available smartphones. Bioelectromagnetics Society Annual Meeting. Montpellier, France, 2019.
- [37] Wang N, Blostein SD. Comparison of CP-based single carrier and OFDM with power allocation. *IEEE Transactions on Communications*. 2005;53(3):391–394.